Available online at www.sciencedirect.com
ScienceDirect
Comput. Methods Appl. Mech. Engrg. 283 (2015) 1189–1213
Computer methods in applied mechanics and engineering
www.elsevier.com/locate/cma

Finite-element harmonic experiments to model fractured induced anisotropy in poroelastic media

Juan E. Santos[a,b,c,*], José M. Carcione[d]

[a] *Department of Mathematics, Purdue University, 150 N. University Street, West Lafayette, IN 47907-2067, USA*
[b] *CONICET, Instituto del Gas y del Petróleo, Facultad de Ingeniería, Universidad de Buenos Aires, Av. Las Heras 2214 Piso 3 C1127AAR Buenos Aires, Argentina*
[c] *Universidad Nacional de La Plata, La Plata, Argentina*
[d] *Istituto Nazionale di Oceanografia e di Geofisica Sperimentale (OGS), Borgo Grotta Gigante 42c, 34010 Sgonico, Trieste, Italy*

Received 10 March 2014; received in revised form 12 August 2014; accepted 14 August 2014
Available online 27 August 2014

Highlights

- We present finite element procedures to model the response of aligned fractures in fluid-saturated poroelastic materials.
- We derive *a priori* error estimates for the finite element procedures.
- We analyze fracture induced velocity and attenuation in heterogeneous fractured poroelastic materials.

Abstract

Fractures in a fluid-saturated poroelastic – Biot – medium can be modeled as very thin highly permeable and compliant layers within a porous background. A Biot medium containing a dense set of aligned fractures behaves as an effective transversely isotropic and viscoelastic (TIV) medium at the macroscale when the predominant wavelength is much larger than the average distance between fractures. One important mechanism in Biot media at seismic frequencies is wave-induced fluid flow generated by fast compressional waves at mesoscopic-scale heterogeneities, generating slow diffusion-type Biot waves. In this work, we present and analyze a collection of time-harmonic finite element experiments that take into account the effects of the presence of aligned fractures and interlayer fluid flow occurring at the mesoscale, allowing us to determine the complex and frequency dependent stiffnesses of the effective TIV medium at the macroscale.

These numerical upscaling experiments are defined as boundary value problems on representative samples of the fractured material, with boundary conditions associated with compressibility and shear tests, which are solved using the finite element (FE) method. The FE space chosen to discretize each component of the solid displacement vector is that of globally continuous piecewise bilinear functions, while for the fluid phase the vector part of the Raviart–Thomas–Nedelec space of zero order is employed. We present results on the uniqueness of the solution of the continuous and discrete problems, and derive optimal *a priori* energy error estimates. First, the numerical results are validated with those of a theory valid for fluid flow perpendicular to the fracture layering and independent of the loading direction, so that the attenuation mechanism can be represented by a single relaxation function. Then, the methodology is applied to cases for which no analytical solutions are available, such as a fractured Biot medium saturated

* Corresponding author at: Department of Mathematics, Purdue University, 150 N. University Street, West Lafayette, Indiana, 47907-2067, USA. Tel.: +1 765 494 1925; fax: +1 765 494 0548.
E-mail addresses: santos@math.purdue.edu (J.E. Santos), jcarcione@inogs.it (J.M. Carcione).

http://dx.doi.org/10.1016/j.cma.2014.08.016

with brine and patches of CO_2 and a brine saturated sample of uniform background and fractures with fractal variations in their petrophysical properties.

Keywords: Fractures; Poroelasticity; Finite elements; Anisotropy; Velocity dispersion; Attenuation

1. Introduction

Fractured hydrocarbon reservoirs have been the subject of interest in exploration and production geophysics, since generally, natural fractures control the permeability of the reservoir [1]. In geophysical prospecting and reservoir development, knowledge of fracture orientation, densities and sizes is essential since these factors control hydrocarbon production [2]. This is also important in CO_2 storage in geological formations to monitor the injected plumes as faults and fractures are generated, where CO_2 can leak to the surface [3]. One of the important mechanisms of seismic attenuation in fluid-saturated porous media is wave-induced fluid flow, by which the fast compressional wave is converted to slow (diffusive) Biot waves at mesoscopic-scale heterogeneities, which are larger than the pore size but much smaller than the predominant wavelengths of the fast compressional and shear waves [5,15].

White et al. [4] were the first to introduce the mesoscopic-loss mechanism in the framework of Biot theory considering alternating thin poroelastic layers along the direction perpendicular to the layering plane [5]. Gelinsky and Shapiro [6] obtained the relaxed and unrelaxed stiffnesses of the equivalent poro-viscoelastic medium to a finely layered horizontally homogeneous material. Krzikalla and Müller [7] combined the two previous models to obtain the five complex and frequency-dependent stiffnesses of the equivalent TIV medium. Their approach assumes a 1D character of the fluid pressure equilibration process which generates diffusive modes from the fast compressional wave, i.e., the fluid-flow direction is perpendicular to the fracture layering. As a consequence, compressional waves travelling horizontally or vertically or shear waves will generate fluid pressure in such a way as to maintain its distribution. Thus, the model considers only one relaxation function, corresponding to the symmetry-axis compressional wave stiffness. These assumptions fail for heterogeneous layers, where the propagation of waves may depend on direction.

A planar fracture embedded in a fluid-saturated poroelastic background is a particular case of the thin layer problem, when one of the layers is very thin, highly permeable and compliant. A dense set of horizontal fractures in a fluid-saturated poroelastic medium behaves as a TIV medium when the average fracture distance is much smaller than the predominant wavelength of the travelling waves. This leads to frequency and angular variations of velocity and attenuation of seismic waves. An analysis of wave anelasticity and anisotropy in fractured poroelastic rocks is presented in [8].

FE harmonic compressibility and shear tests are first presented in [9] to obtain a viscoelastic medium long-wavelength equivalent to a highly heterogeneous isotropic sample. Then, in [10] and [11] the procedure is extended to determine long-wave equivalent media to finely layered viscoelastic materials. Among other works employing numerical simulations to analyze dispersion, attenuation and anisotropy in Biot media we mention the works by Saenger et al. [12] and Wenzlau et al. [13].

This work presents and analyzes a collection of time-harmonic finite element experiments defined on fluid-saturated isotropic poroelastic samples having a dense set of horizontal fractures modeled as very thin layers. The experiments take into account both the effects fractures and interlayer fluid flow occurring at the mesoscale. Each experiment is defined at the continuous level as a boundary value problem defined in the space-frequency domain, with boundary conditions representing compressibility and shear tests that are solved using the FE method. To discretize each component of the solid displacement vector we employ the space of globally continuous piecewise bilinear functions over a quasi-regular partition of the computational domain. For the fluid phase, the vector part of the Raviart–Thomas–Nedelec space of zero order is used [14]. First, we demonstrate the uniqueness of the solution of the continuous and discrete boundary value problems associated with each experiment and derive *a priori* error estimates in the energy norm for the FE solutions. These estimates are optimal for the assumed regularity of the solution.

First, we present the validation of the FE procedure by comparison with the analytical solutions provided in [7] for a brine saturated homogeneous sample having a dense set of horizontal fractures. Then, the methodology is applied in two cases for which no analytical solutions are available, namely patchy brine–CO_2 saturated samples and

brine-saturated samples with fractures having fractal variations in the petrophysical properties. We analyze the effect of these fluid and frame heterogeneities on the attenuation and dispersion of the quasi-compressional wave (qP wave), vertically polarized quasi-shear wave (qSV wave) and horizontally polarized shear wave (SH wave).

2. The Biot model and the equivalent TIV medium

Let us consider isotropic fluid-saturated poroelastic layers and let $\mathbf{u}_s(\mathbf{x}) = (u_{s,1}, u_{s,2}, u_{s,3})$ and $\mathbf{u}_f(\mathbf{x}) = (u_{f,1}, u_{f,2}, u_{f,3})$ indicate the time Fourier transform of the displacement vector of the solid and fluid relative to the solid frame, respectively. Here, if $\mathbf{U}_f$ denotes the fluid displacement vector, $\mathbf{u}_f = \phi(\mathbf{U}_f - \mathbf{u}_s)$, where ϕ is the porosity.

Set $\mathbf{u} = (\mathbf{u}_s, \mathbf{u}_f)$ and let $\boldsymbol{\sigma}(\mathbf{u})$ and $p_f(\mathbf{u})$ denote the time Fourier transform of the total stress and the fluid pressure, respectively, and let $\mathbf{e}(\mathbf{u}_s)$ be the strain tensor of the solid phase. On each plane layer n in a sequence of N layers, the frequency-domain stress–strain relations are [15]

$$\sigma_{kl}(\mathbf{u}) = 2\mu\, e_{kl}(\mathbf{u}_s) + \delta_{kl}\left(\lambda_G\, \nabla\cdot\mathbf{u}_s + \alpha M \nabla\cdot\mathbf{u}_f\right), \tag{1}$$

$$p_f(\mathbf{u}) = -\alpha M \nabla\cdot\mathbf{u}_s - M\nabla\cdot\mathbf{u}_f. \tag{2}$$

The coefficient μ is the shear modulus of the bulk material, considered to be equal to the shear modulus of the dry matrix. The other coefficients in (1)–(2) can be obtained from the relations [15]

$$\lambda_G = K_G - \frac{2}{3}\mu, \quad K_G = K_m + \alpha^2 M, \tag{3}$$

$$\alpha = 1 - \frac{K_m}{K_s}, \quad M = \left(\frac{\alpha-\phi}{K_s} + \frac{\phi}{K_f}\right)^{-1},$$

where K_s, K_m and K_f denote the bulk moduli of the solid grains, dry matrix and saturant fluid, respectively.

Let us define the differential operator $\mathcal{L}(\mathbf{u})$ and the matrix $\mathcal{B} \in \mathbf{R}^4$ as follows:

$$\mathcal{L}(\mathbf{u}) = \left(\nabla\cdot\boldsymbol{\sigma}(\mathbf{u}), \nabla p_f(\mathbf{u})\right), \quad \mathcal{B} = \begin{pmatrix} 0I_2 & 0I_2 \\ 0I_2 & \dfrac{\eta}{\kappa} I_2 \end{pmatrix}, \tag{4}$$

where I_2 is the 2×2 identity matrix, η is the fluid viscosity and κ is the frame permeability. Denoting by $\omega = 2\pi f$ the angular frequency, Biot's equations in the diffusive range, stated in the space-frequency domain are (in the absence of external sources)

$$i\omega\mathcal{B}\mathbf{u} - \mathcal{L}(\mathbf{u}) = 0, \tag{5}$$

where $i = \sqrt{-1}$. Let us consider x_1 and x_3 as the horizontal and vertical coordinates, respectively. As shown by Gelinsky and Shapiro [6], the medium behaves as a TI medium with a vertical symmetry axis (the x_3-axis) at long wavelengths. They obtain the relaxed and unrelaxed limits, i.e., the low- and high-frequency limit real-valued stiffnesses, respectively. Assuming a 1D character of the fluid pressure equilibration process, Krzikalla and Müller [7] present a model to obtain the five complex and frequency-dependent stiffnesses p_{IJ}, $I, J = 1, \ldots, 6$, of the equivalent TIV medium that is included in Appendix A.

Denote by $\tau_{ij}(\widetilde{\mathbf{u}}_s)$ and $\epsilon_{ij}(\widetilde{\mathbf{u}}_s)$ the stress and strain tensor components of the equivalent TIV medium, where $\widetilde{\mathbf{u}}_s$ denotes the solid displacement vector at the macroscale. The corresponding stress–strain relations, stated in the space-frequency domain, are [16,15]

$$\tau_{11}(\widetilde{\mathbf{u}}_s) = p_{11}\,\epsilon_{11}(\widetilde{\mathbf{u}}_s) + p_{12}\,\epsilon_{22}(\widetilde{\mathbf{u}}_s) + p_{13}\,\epsilon_{33}(\widetilde{\mathbf{u}}_s), \tag{6}$$

$$\tau_{22}(\widetilde{\mathbf{u}}_s) = p_{12}\,\epsilon_{11}(\widetilde{\mathbf{u}}_s) + p_{11}\,\epsilon_{22}(\widetilde{\mathbf{u}}_s) + p_{13}\,\epsilon_{33}(\widetilde{\mathbf{u}}_s), \tag{7}$$

$$\tau_{33}(\widetilde{\mathbf{u}}_s) = p_{13}\,\epsilon_{11}(\widetilde{\mathbf{u}}_s) + p_{13}\,\epsilon_{22}(\widetilde{\mathbf{u}}_s) + p_{33}\,\epsilon_{33}(\widetilde{\mathbf{u}}_s), \tag{8}$$

$$\tau_{23}(\widetilde{\mathbf{u}}_s) = 2\,p_{55}\,\epsilon_{23}(\widetilde{\mathbf{u}}_s), \tag{9}$$

$$\tau_{13}(\widetilde{\mathbf{u}}_s) = 2\,p_{55}\,\epsilon_{13}(\widetilde{\mathbf{u}}_s), \tag{10}$$

$$\tau_{12}(\widetilde{\mathbf{u}}_s) = 2\,p_{66}\,\epsilon_{12}(\widetilde{\mathbf{u}}_s). \tag{11}$$

In (6)–(11) we have assumed a closed system. This can be done for the undrained composite medium, for which the variation of fluid content $\zeta = -\nabla \cdot \mathbf{u}_f$ is equal to zero. This approach provides the complex velocities of the fast qP, qSV and SH modes. The p_{IJ} are the complex and frequency-dependent Voigt stiffnesses to be determined with the harmonic experiments. In the next sections we present and analyze a FE procedure to determine the coefficients in (6)–(11) and the corresponding phase velocities and quality factors. These properties, which depend on frequency and propagation direction, are given in Appendix B.

3. Determination of the stiffnesses

Here we show how that stiffnesses p_{IJ} can be determined by applying a collection of compressibility and shear tests on a 2D representative sample $\Omega = (0, L)^2$ of boundary $\Gamma = \partial\Omega$ of the fractured poroelastic material in the (x_1, x_3)-plane.

Set $\Gamma = \Gamma^L \cup \Gamma^B \cup \Gamma^R \cup \Gamma^T$, where

$$\Gamma^L = \{(x_1, x_3) \in \Gamma : x_1 = 0\}, \quad \Gamma^R = \{(x_1, x_3) \in \Gamma : x_1 = L\},$$
$$\Gamma^B = \{(x_1, x_3) \in \Gamma : x_3 = 0\}, \quad \Gamma^T = \{(x_1, x_3) \in \Gamma : x_3 = L\}.$$

Denote by $\boldsymbol{\nu}$ the unit outer normal on Γ and let $\boldsymbol{\chi}$ be a unit tangent on Γ so that $\{\boldsymbol{\nu}, \boldsymbol{\chi}\}$ is an orthonormal system on Γ.

(i) To determine the complex coefficient p_{33} let us consider the solution of (5) in Ω together with the following boundary conditions

$$\boldsymbol{\sigma}(\mathbf{u})\boldsymbol{\nu} \cdot \boldsymbol{\nu} = -\Delta P, \quad (x_1, x_3) \in \Gamma^T, \tag{12}$$
$$\boldsymbol{\sigma}(\mathbf{u})\boldsymbol{\nu} \cdot \boldsymbol{\chi} = 0, \quad (x_1, x_3) \in \Gamma, \tag{13}$$
$$\mathbf{u}_s \cdot \boldsymbol{\nu} = 0, \quad (x_1, x_3) \in \Gamma^L \cup \Gamma^R \cup \Gamma^B, \tag{14}$$
$$\mathbf{u}_f \cdot \boldsymbol{\nu} = 0, \quad (x_1, x_3) \in \Gamma. \tag{15}$$

Denoting by V the original volume of the sample, its (complex) oscillatory volume change, $\Delta V(\omega)$, allows us to define p_{33} by using the relation

$$\frac{\Delta V(\omega)}{V} = -\frac{\Delta P}{p_{33}(\omega)}, \tag{16}$$

valid for a viscoelastic homogeneous medium in the quasistatic case.

After solving (5) with the boundary conditions (12)–(15), the vertical displacements $u_{s,3}(x_1, L, \omega)$ on Γ^T allow us to obtain an average vertical displacement $u^T_{s,3}(\omega)$ suffered by the boundary Γ^T. Then, for each frequency ω, the volume change produced by the compressibility test can be approximated by $\Delta V(\omega) \approx L u^T_{s,3}(\omega)$, which enable us to compute $p_{33}(\omega)$ by using the relation (16).

(ii) To determine p_{11}, we solve (5) in Ω together with the boundary conditions

$$\boldsymbol{\sigma}(\mathbf{u})\boldsymbol{\nu} \cdot \boldsymbol{\nu} = -\Delta P, \quad (x_1, x_3) \in \Gamma^R, \tag{17}$$
$$\boldsymbol{\sigma}(\mathbf{u})\boldsymbol{\nu} \cdot \boldsymbol{\chi} = 0, \quad (x_1, x_3) \in \Gamma, \tag{18}$$
$$\mathbf{u}_s \cdot \boldsymbol{\nu} = 0, \quad (x_1, x_3) \in \Gamma^L \cup \Gamma^B \cup \Gamma^T, \tag{19}$$
$$\mathbf{u}_f \cdot \boldsymbol{\nu} = 0, \quad (x_1, x_3) \in \Gamma. \tag{20}$$

In this experiment $\epsilon_{33}(\mathbf{u}_s) = \epsilon_{22}(\mathbf{u}_s) = \nabla \cdot \mathbf{u}_f = 0$ and from (6) we see that this experiment determines p_{11} as indicated for p_{33} measuring the oscillatory volume change.

(iii) To determine p_{55} let us consider the solution of (5) in Ω with the following boundary conditions

$$-\boldsymbol{\sigma}(\mathbf{u})\boldsymbol{\nu} = \mathbf{g}, \quad (x_1, x_3) \in \Gamma^T \cup \Gamma^L \cup \Gamma^R, \tag{21}$$
$$\mathbf{u}_s = 0, \quad (x_1, x_3) \in \Gamma^B, \tag{22}$$
$$\mathbf{u}_f \cdot \boldsymbol{\nu} = 0, \quad (x_1, x_3) \in \Gamma, \tag{23}$$

where

$$\mathbf{g} = \begin{cases} (0, \Delta G), & (x_1, x_3) \in \Gamma^L, \\ (0, -\Delta G), & (x_1, x_3) \in \Gamma^R, \\ (-\Delta G, 0), & (x_1, x_3) \in \Gamma^T. \end{cases}$$

The change in shape of the rock sample allows to obtain $p_{55}(\omega)$ by using the relation

$$\mathrm{tg}(\beta(\omega)) = \frac{\Delta G}{p_{55}(\omega)}, \tag{24}$$

where $\beta(\omega)$ is the departure angle between the original positions of the lateral boundaries and those after applying the shear stresses (see, for example, [17]). Eq. (24) holds for this experiment in a viscoelastic homogeneous media in the quasistatic approximation.

The horizontal displacements $u_{s,1}(x_1, L, \omega)$ at the top boundary Γ^T allow us to obtain, for each frequency, an average horizontal displacement $u^T_{s,1}(\omega)$ suffered by the boundary Γ^T. This average value allows us to approximate the change in shape suffered by the sample, given by $\mathrm{tg}(\beta(\omega)) \approx u^T_{s,1}(\omega)/L$, which from (24) let us estimate $p_{55}(\omega)$.

(v) To determine p_{13} we solve (5) in Ω with the boundary conditions

$$\boldsymbol{\sigma}(\mathbf{u})\boldsymbol{\nu} \cdot \boldsymbol{\nu} = -\Delta P, \quad (x_1, x_3) \in \Gamma^R \cup \Gamma^T, \tag{25}$$

$$\boldsymbol{\sigma}(\mathbf{u})\boldsymbol{\nu} \cdot \boldsymbol{\chi} = 0, \quad (x_1, x_3) \in \Gamma, \tag{26}$$

$$\mathbf{u}_s \cdot \boldsymbol{\nu} = 0, \quad (x_1, x_3) \in \Gamma^L \cup \Gamma^B, \tag{27}$$

$$\mathbf{u}_f \cdot \boldsymbol{\nu} = 0, \quad (x_1, x_3) \in \Gamma. \tag{28}$$

Thus, in this experiment $\epsilon_{22}(\mathbf{u}_s) = \nabla \cdot \mathbf{u}_f = 0$, and from (6) and (8) we get

$$\begin{aligned} \tau_{11} &= c_{11}\epsilon_{11} + c_{13}\epsilon_{33} \\ \tau_{33} &= c_{13}\epsilon_{11} + c_{33}\epsilon_{33}, \end{aligned} \tag{29}$$

where ϵ_{11} and ϵ_{33} are the (macroscale) strain components at the right lateral side and top side of the sample, respectively. Then from (29) and the fact that $\tau_{11} = \tau_{33} = -\Delta P$ (c.f. (25)) we obtain $p_{13}(\omega)$ as

$$p_{13}(\omega) = \frac{c_{11}\epsilon_{11} - c_{33}\epsilon_{33}}{\epsilon_{11} - \epsilon_{33}}. \tag{30}$$

(iv) To determine p_{66}, since this stiffness is associated with shear waves travelling in the (x_1, x_2)-plane, we consider a homogeneous horizontal slab in the x_2-direction and a homogeneous sample $\Omega_2 = (0, L)^2$ in the (x_1, x_2)-plane, with boundary $\Gamma_2 = \Gamma_2^L \cup \Gamma_2^B \cup \Gamma_2^R \cup \Gamma_2^T$, where

$$\begin{aligned} \Gamma_2^L &= \{(x_1, x_2) \in \Gamma : x_1 = 0\}, \quad \Gamma_2^R = \{(x_1, x_2) \in \Gamma : x_1 = L\}, \\ \Gamma_2^B &= \{(x_1, x_2) \in \Gamma : x_2 = 0\}, \quad \Gamma^T = \{(x_1, x_2) \in \Gamma : x_2 = L\}. \end{aligned}$$

Then let us consider the solution of (5) in Ω_2 with the following boundary conditions

$$-\boldsymbol{\sigma}(\mathbf{u})\boldsymbol{\nu} = \mathbf{g}_2, \quad (x_1, x_2) \in \Gamma_2^T \cup \Gamma_2^L \cup \Gamma_2^R, \tag{31}$$

$$\mathbf{u}_s = 0, \quad (x_1, x_2) \in \Gamma_2^B, \tag{32}$$

$$\mathbf{u}_f \cdot \boldsymbol{\nu} = 0, \quad (x_1, x_2) \in \Gamma, \tag{33}$$

where

$$\mathbf{g}_2 = \begin{cases} (0, \Delta G), & (x_1, x_2) \in \Gamma_2^L, \\ (0, -\Delta G), & (x_1, x_2) \in \Gamma_2^R, \\ (-\Delta G, 0), & (x_1, x_2) \in \Gamma_2^T. \end{cases}$$

Then, we proceed as indicated for $p_{55}(\omega)$.

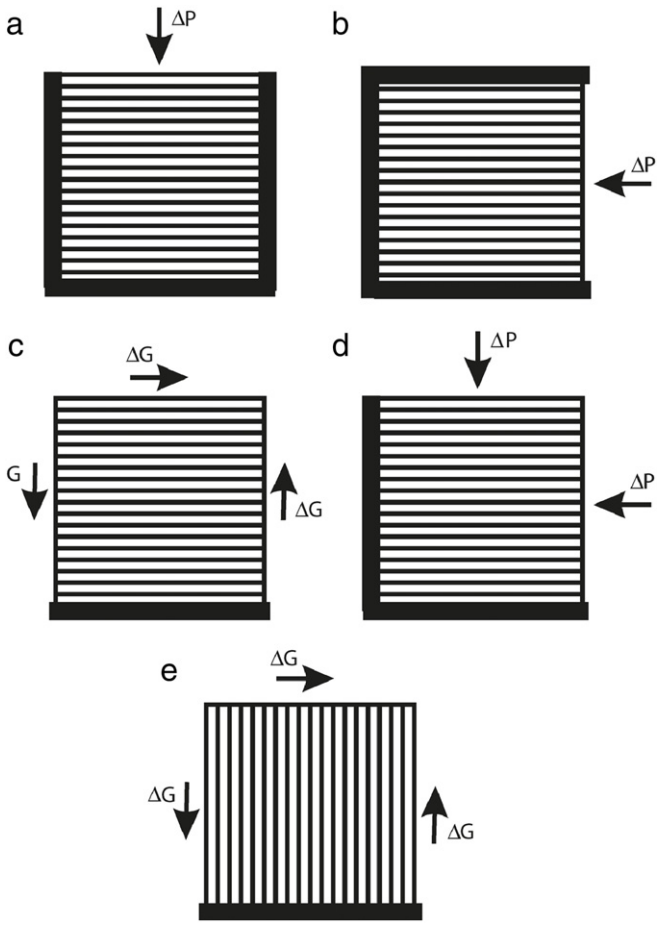

Fig. 1. Oscillatory tests performed to obtain p_{33} (a), p_{11} (b), p_{55} (c), p_{13} (d) and p_{66} (e). The orientation of the layers and the directions of the applied stresses are indicated. The thick black lines at the edges indicate rigid boundary conditions (zero displacements).

The stiffnesses coefficients p_{IJ} allow us to calculate the wave velocities and quality factors of the effective TIV medium as explained in Appendix B.

Fig. 1(a)–(e) illustrate the five experiments needed to compute the stiffnesses components. In Fig. 1(a) and (b) we show how to compute p_{33} and p_{11} using the boundary conditions (12)–(15) and (17)–(20), respectively. On the other hand, using the boundary conditions (21)–(23), we obtain the stiffness p_{55} by performing the experiment shown in 1(c) and the stiffness p_{66} with the experiment shown in 1(e) (boundary conditions (31)–(33)). Finally, Fig. 1(d) displays the experiment to determine p_{13} using the boundary conditions (25)–(28).

4. A variational formulation

In order to state a variational formulation we need to introduce some notation. For $X \subset \mathbb{R}^d$ with boundary ∂X, let $(\cdot,\cdot)_X$ and $\langle\cdot,\cdot\rangle_{\partial X}$ denote the complex $L^2(X)$ and $L^2(\partial X)$ inner products for scalar, vector, or matrix valued functions. Also, for $s \in \mathbb{R}$, $\|\cdot\|_{s,X}$ and $|\cdot|_{s,X}$ will denote the usual norm and seminorm for the Sobolev space $H^s(X)$, [18]. In addition, if $X = \Omega$ or $\partial X = \Gamma$, the subscripts X and Γ may be omitted such that $(\cdot,\cdot) = (\cdot,\cdot)_\Omega$ or $\langle\cdot,\cdot\rangle = \langle\cdot,\cdot\rangle_\Gamma$.

Let us introduce the following closed subspaces of $[H^1(\Omega)]^2$ and $[H^1(\Omega_2)]^2$:

$$\mathcal{W}_{11}(\Omega) = \{\mathbf{v} \in [H^1(\Omega)]^2 : \mathbf{v}\cdot\boldsymbol{\nu} = 0 \text{ on } \Gamma^B \cup \Gamma^T \cup \Gamma^L\},$$

$$\mathcal{W}_{33}(\Omega) = \{\mathbf{v} \in [H^1(\Omega)]^2 : \mathbf{v}\cdot\boldsymbol{\nu} = 0 \text{ on } \Gamma^L \cup \Gamma^R \cup \Gamma^B\},$$

$$\mathcal{W}_{13}(\Omega) = \{\mathbf{v} \in [H^1(\Omega)]^2 : \ \mathbf{v} \cdot \boldsymbol{\nu} = 0 \text{ on } \Gamma^L \cup \Gamma^B\},$$

$$\mathcal{W}_{55}(\Omega) = \{\mathbf{v} \in [H^1(\Omega)]^2 : \ \mathbf{v} = 0 \text{ on } \Gamma^B\},$$

$$\mathcal{W}_{66}(\Omega_2) = \{\mathbf{v} \in [H^1(\Omega_2)]^2 : \ \mathbf{v} = 0 \text{ on } \Gamma_2^B\}.$$

Also, let

$$H_0(\text{div}; \Omega) = \{\mathbf{v} \in H(\text{div}; \Omega) : \ \mathbf{v} \cdot \boldsymbol{\nu} = 0 \text{ on } \Gamma\},$$

$$H_0(\text{div}; \Omega_2) = \{\mathbf{v} \in H(\text{div}; \Omega_2) : \ \mathbf{v} \cdot \boldsymbol{\nu} = 0 \text{ on } \Gamma_2\},$$

$$H^1(\text{div}; \Omega) = \{\mathbf{v} \in [H^1(\Omega)]^2 : \ \nabla \cdot \mathbf{v} \in H^1(\Omega)\},$$

and for $(I, J) = (1, 1), (3, 3), (1, 3), (5, 5)$ let

$$\mathcal{Z}_{IJ}(\Omega) = \mathcal{W}_{IJ}(\Omega) \times H_0(\text{div}; \Omega).$$

Also, let

$$\mathcal{Z}_{66}(\Omega_2) = \mathcal{W}_{66}(\Omega_2) \times H_0(\text{div}; \Omega_2).$$

To obtain our variational formulation associated with p_{33}, multiply (5) by $\mathbf{v} = \left(\mathbf{v}_s, \mathbf{v}_f\right) \in \mathcal{Z}_{33}(\Omega)$, use integration by parts and apply the boundary conditions (12)–(15) to get *the weak form*: find $\mathbf{u}^{(33)} = (\mathbf{u}_s^{(33)}, \mathbf{u}_f^{(33)}) \in \mathcal{Z}_{33}(\Omega)$ such that

$$\begin{aligned} \Lambda(\mathbf{u}^{(33)}, \mathbf{v}) &\equiv i\omega \left(\frac{\eta}{\kappa}\mathbf{u}_f^{(33)}, \mathbf{v}_f\right) + \sum_{s,t} \left(\sigma_{st}(\mathbf{u}^{(33)}), e_{st}(\mathbf{v}_s)\right) - \left(p_f(\mathbf{u}^{(33)}), \nabla \cdot \mathbf{v}_f\right) \\ &= -\langle \Delta P, \mathbf{v}_s \cdot \boldsymbol{\nu} \rangle_{\Gamma^T}, \quad \forall\ \mathbf{v} = \left(\mathbf{v}_s, \mathbf{v}_f\right) \in \mathcal{Z}_{33}(\Omega). \end{aligned} \tag{34}$$

Note that in (34), we can write

$$\sum_{l=1}^{2} \sum_{s,t} \left(\sigma_{st}(\mathbf{u}^{(33)}), e_{st}(\mathbf{v}^s)\right) - \left(p_f(\mathbf{u}^{(33)}), \nabla \cdot \mathbf{v}^f\right)_{R^{(l)}} = \left(\mathbf{E}\, \widetilde{\mathbf{e}}(\mathbf{u}^{(33)}), \widetilde{e}(\mathbf{v})\right). \tag{35}$$

In (35), the matrix $\mathbf{E}$ and the column vector $\widetilde{\mathbf{e}}(\mathbf{u}^{(33)})$ are defined by

$$\mathbf{E} = \begin{pmatrix} \lambda_G + 2\mu & \lambda_G & \alpha M & 0 \\ \lambda_G & \lambda_G + 2\mu & \alpha M & 0 \\ \alpha M & \alpha M & M & 0 \\ 0 & 0 & 0 & 4\mu \end{pmatrix}, \qquad \widetilde{\mathbf{e}}(\mathbf{u}^{(33)}) = \begin{pmatrix} e_{11}(\mathbf{u}_s^{(33)}) \\ e_{33}(\mathbf{u}_s^{(33)}) \\ \nabla \cdot \mathbf{u}_f^{(33)} \\ e_{13}(\mathbf{u}_s^{(33)}) \end{pmatrix}. \tag{36}$$

Note that $\mathbf{E}$ is positive definite since it is associated with the strain energy density.

Thus we can state (34) in the equivalent form: find $\mathbf{u}^{(33)} = (\mathbf{u}_s^{(33)}, \mathbf{u}_f^{(33)}) \in \mathcal{Z}_{33}(\Omega)$ such that

$$\Lambda(\mathbf{u}^{(33)}, \mathbf{v}) = i\omega \left(\frac{\eta}{\kappa}\mathbf{u}_f^{(33)}, \mathbf{v}_f\right) + \left(\mathbf{E}\, \widetilde{\mathbf{e}}(\mathbf{u}^{(33)}), \widetilde{\mathbf{e}}(\mathbf{v})\right). \tag{37}$$

Similarly, we obtain the variational formulations for the other p_{IJ}'s:

- $p_{(11)}$:
  Find $\mathbf{u}^{(11)} = (\mathbf{u}_s^{(11)}, \mathbf{u}_f^{(11)}) \in \mathcal{Z}_{11}(\Omega)$ such that

$$\Lambda(\mathbf{u}^{(11)}, \mathbf{v}) = -\langle \Delta P, \mathbf{v}_s \cdot \boldsymbol{\nu} \rangle_{\Gamma^R}, \quad \forall \mathbf{v} = \left(\mathbf{v}_s, \mathbf{v}_f\right) \in \mathcal{Z}_{11}(\Omega). \tag{38}$$

- $p_{(13)}$:
  Find $\mathbf{u}^{(13)} = (\mathbf{u}_s^{(13)}, \mathbf{u}_f^{(13)}) \in \mathcal{Z}_{13}(\Omega)$ such that

$$\Lambda(\mathbf{u}^{(13)}, \mathbf{v}) = -\langle \Delta P, \mathbf{v}_s \cdot \boldsymbol{\nu} \rangle_{\Gamma^R \cup \Gamma^T}, \quad \forall \mathbf{v} = \left(\mathbf{v}_s, \mathbf{v}_f\right) \in \mathcal{Z}_{13}(\Omega). \tag{39}$$

- $p_{(55)}$:
  Find $\mathbf{u}^{(55)} = (\mathbf{u}_s^{(55)}, \mathbf{u}_f^{(55)}) \in \mathcal{Z}_{55}(\Omega)$ such that

$$\Lambda(\mathbf{u}^{(55)}, \mathbf{v}) = -\langle \mathbf{g}, \mathbf{v}_s \rangle_{\Gamma^R \cup \Gamma^T}, \quad \forall \mathbf{v} = (\mathbf{v}_s, \mathbf{v}_f) \in \mathcal{Z}_{55}(\Omega). \tag{40}$$

- $p_{(66)}$:
  Find $\mathbf{u}^{(66)} = (\mathbf{u}_s^{(66)}, \mathbf{u}_f^{(66)}) \in \mathcal{Z}_{66}(\Omega_2)$ such that

$$\Lambda(\mathbf{u}^{(66)}, \mathbf{v}) = -\langle \mathbf{g}_2, \mathbf{v}_s \rangle_{\Gamma^R \cup \Gamma^T}, \quad \forall \mathbf{v} = (\mathbf{v}_s, \mathbf{v}_f) \in \mathcal{Z}_{66}(\Omega_2). \tag{41}$$

4.1. Uniqueness of the solution of the variational problems

The five boundary-value problems formulated above are associated with second-order operators having boundary data in $L^2(\Omega)$. Existence will be assumed for the solution of these problems. Also, following [19] we will assume that $\mathbf{u}_s^{(IJ)} \in [H^{3/2}]^2$. On the other hand, it will be assumed that $\mathbf{u}_f^{(IJ)} \in H^1(\text{div}; \Omega)$. These assumptions will be used in the proof of the theorem stated below.

Theorem 1. *Assume that* $\mathbf{u}_s^{(IJ)} \in [H^{3/2}(\Omega)]^2, \mathbf{u}_f^{(IJ)} \in H^1(\text{div}; \Omega)$ *for* $(I, J) = (1, 1), (3, 3), (1, 3), (5, 5)$ *and that* $\mathbf{u}_s^{(66)} \in [H^{3/2}(\Omega_2)]^2, \mathbf{u}_f^{(66)} \in H^1(\text{div}; \Omega_2)$. *Also assume that the matrix* $\mathbf{E}$ *in (36) is positive definite. Then the solution of problems (37)–(41) is unique.*

Proof. To analyze the uniqueness of the solution of (37), set $\Delta P = 0$ and choose $\mathbf{v} = \mathbf{u}^{(33)}$ in (37) to obtain the equation

$$i\omega \left(\frac{\eta}{\kappa} \mathbf{u}_f^{(33)}, \mathbf{u}_f^{(33)} \right) + \left(\mathbf{E}\, \widetilde{\mathbf{e}}(\mathbf{u}^{(33)}), \widetilde{\mathbf{e}}(\mathbf{u}^{(33)}) \right) = 0. \tag{42}$$

Choose the imaginary part in (42) to conclude that

$$\|\mathbf{u}_f^{(33)}\|_0 = 0. \tag{43}$$

Using (43) in (42) we obtain

$$\left(\widehat{\mathbf{E}}\, \widehat{\mathbf{e}}(\mathbf{u}_s^{(33)}), \widehat{\mathbf{e}}(\mathbf{u}_s^{(33)}) \right) = 0, \tag{44}$$

where

$$\widehat{\mathbf{E}} = \begin{pmatrix} \lambda_G + 2\mu & \lambda_G & 0 \\ \lambda_G & \lambda_G + 2\mu & 0 \\ 0 & 0 & 4\mu \end{pmatrix}, \quad \widehat{\mathbf{e}}(\mathbf{u}_s^{(33)}) = \begin{pmatrix} e_{11}(\mathbf{u}_s^{(33)}) \\ e_{33}(\mathbf{u}_s^{(33)}) \\ e_{13}(\mathbf{u}_s^{(33)}) \end{pmatrix}. \tag{45}$$

Next, since the matrix $\mathbf{E}$ is positive, so it is the matrix $\widehat{\mathbf{E}}$, which from (44) allow us to conclude that

$$\|e_{11}(\mathbf{u}_s^{(33)})\|_0 = \|e_{33}(\mathbf{u}_s^{(33)})\|_0 = \|e_{13}(\mathbf{u}_s^{(33)})\|_0 = 0. \tag{46}$$

Now use the Sobolev embedding [18]

$$H^{3/2}(\Omega) \to C^0(\overline{\Omega}) \tag{47}$$

and (46) to see that for some constants A, B, C

$$u_{s,1}^{(33)}(x_1, x_3) = Cx_3 + B, \qquad u_{s,3}^{(33)}(x_1, x_3) = -Cx_1 + B, \quad \forall (x_1, x_3) \in \overline{\Omega}. \tag{48}$$

Next using the boundary condition (14) we see that $A = B = C = 0$, so that

$$\mathbf{u}_s^{(33)} = 0, \quad \in \overline{\Omega}. \tag{49}$$

Combining (43) and (48) we conclude that uniqueness holds for the solution of (37). Uniqueness for the solution of (38) and (39) follows with the same argument.

Let us analyze uniqueness for the solution of (40). Set $\Delta P = 0$ and choose $\mathbf{v} = \mathbf{u}^{(55)}$ in (40). Repeating the argument given to show uniqueness for $\mathbf{v} = \mathbf{u}^{(33)}$ we obtain

$$\|\mathbf{u}_f^{(55)}\|_0 = 0, \tag{50}$$
$$\|e_{11}(\mathbf{u}_s^{(55)})\|_0 = \|e_{33}(\mathbf{u}_s^{(55)})\|_0 = \|e_{13}(\mathbf{u}_s^{(55)})\|_0 = 0.$$

Next, note that since elements in $\mathcal{Z}_{55}(\Omega)$ vanish on Γ^B,

$$\|\mathbf{v}\| = \left(\sum_{k,l}\int_\Omega |\varepsilon_{kl}(\mathbf{v})|^2 d\Omega\right)^{1/2} \tag{51}$$

defines a norm on $\mathcal{Z}_{55}(\Omega)$ equivalent to the H^1-norm in Ω, [20]. Thus from (50) we see that

$$\|\mathbf{u}_s^{(55)}\|_1 = 0. \tag{52}$$

From (50) and (52) we see that uniqueness holds for the solution of (40). Uniqueness for the solution of (41) follows with identical argument. This completes the proof.

5. The finite element method

Let $\mathcal{T}^h(\Omega)$ be a non-overlapping partition of Ω into rectangles Ω_j of diameter bounded by h such that $\overline{\Omega} = \cup_J^J \overline{\Omega}_j$. Denote by $\Gamma_{jk} = \partial\Omega_j \cap \partial\Omega_k$ the common side of two adjacent rectangles Ω_j and Ω_k. Also, let $\Gamma_j = \partial\Omega_j \cap \Gamma$.

We employ the space of globally continuous piecewise bilinear polynomials, denoted below by $\mathcal{W}_{33}^h(\Omega)$ to approximate each component of the solid displacement $\mathbf{u}_s$, while the vector part of the Raviart–Thomas–Nedelec space $\mathcal{V}_{33}^h(\Omega)$ of zero order is used to approximate the fluid displacement vector $\mathbf{u}_f$ [14]. More specifically, let

$$\mathcal{W}_{11}^h(\Omega) = \{\mathbf{v}_s : \mathbf{v}_s|_{\Omega_j} \in [P_{1,1}(\Omega_j)]^2, \mathbf{v}_s \cdot \boldsymbol{\nu} = 0 \text{ on } \Gamma^B \cup \Gamma^T\Gamma^L\} \cap [C^0(\overline{\Omega})]^2,$$
$$\mathcal{W}_{33}^h(\Omega) = \{\mathbf{v}_s : \mathbf{v}_s|_{\Omega_j} \in [P_{1,1}(\Omega_j)]^2, \mathbf{v}_s \cdot \boldsymbol{\nu} = 0 \text{ on } \Gamma^L \cup \Gamma^R\Gamma^B\} \cap [C^0(\overline{\Omega})]^2,$$
$$\mathcal{W}_{13}^h(\Omega) = \{\mathbf{v}_s : \mathbf{v}_s|_{\Omega_j} \in [P_{1,1}(\Omega_j)]^2, \mathbf{v}_s \cdot \boldsymbol{\nu} = 0 \text{ on } \Gamma^L \cup \Gamma^B\} \cap [C^0(\overline{\Omega})]^2,$$
$$\mathcal{W}_{55}^h(\Omega) = \{\mathbf{v}_s : \mathbf{v}_s|_{\Omega_j} \in [P_{1,1}(\Omega_j)]^2, \mathbf{v}_s \cdot \boldsymbol{\nu} = 0 \text{ on } \Gamma^B\} \cap [C^0(\overline{\Omega})]^2$$
$$\mathcal{W}_{66}^h(\Omega_2) = \{\mathbf{v}_s : \mathbf{v}_s|_{\Omega_{2,j}} \in [P_{1,1}(\Omega_{2,j})]^2, \mathbf{v}_s \cdot \boldsymbol{\nu} = 0 \text{ on } \Gamma_2^B\} \cap [C^0(\overline{\Omega})_2]^2$$

be the FE spaces to approximate the solid displacement, and let

$$\mathcal{V}^h(\Omega) = \{\mathbf{v}_f \in H(\text{div};\Omega) : \mathbf{v}_f|_{\Omega_j} \in P_{1,0}(\Omega_j) \times P_{0,1}(\Omega_j),\ \mathbf{v}_f \cdot \boldsymbol{\nu} = 0 \text{ on } \Gamma\}$$
$$\mathcal{V}^h(\Omega_2) = \{\mathbf{v}_f \in H(\text{div};\Omega_2) : \mathbf{v}_f|_{\Omega_{2,j}} \in P_{1,0}(\Omega_{2,j}) \times P_{0,1}(\Omega_{2,j}),\ \mathbf{v}_f \cdot \boldsymbol{\nu} = 0 \text{ on } \Gamma\}$$

be the space to approximate the fluid displacement vector. Here $P_{s,t}$ denotes the polynomials of degree not greater than s in x_1 and not greater than t in x_3.

Then, for $(I, J) = (1, 1), (3, 3), (1, 3), (5, 5)$ let

$$\mathcal{Z}_{IJ}^h(\Omega) = \mathcal{W}_{IJ}^h(\Omega) \times \mathcal{V}^h(\Omega).$$

Also, let

$$\mathcal{Z}_{66}^h(\Omega_2) = \mathcal{W}_{IJ}^h(\Omega_2) \times \mathcal{V}^h(\Omega_2).$$

Next, for $(I, J) = (1, 1), (3, 3), (1, 3), (5, 5)$ let

$$\Pi_{IJ}^h : [H^{3/2}(\Omega)]^2 \to \mathcal{W}_{IJ}^h(\Omega)$$

be the interpolant operators associated with the spaces $\mathcal{W}_{IJ}^h$. More specifically, the degrees of freedom associated with $\Pi_{IJ}^h\mathbf{v}$ are the vertices of the rectangles Ω_j and if b is a common node of the adjacent rectangles Ω_j and Ω_k then $\left(\Pi_{IJ}^h\boldsymbol{\varphi}\right)_j(b) = \left(\Pi_{IJ}^h\boldsymbol{\varphi}\right)_k(b)$, where $\left(\Pi_{IJ}^h\boldsymbol{\varphi}\right)_j$ denotes the restriction of the interpolant $\Pi_{IJ}^h\boldsymbol{\varphi}$ of $\boldsymbol{\varphi}$ to Ω_j.

Also, let

$$Q^h : H_0^1(\mathrm{div};\Omega) \to \mathcal{V}^h(\Omega)$$

be the projection defined by

$$\left\langle (Q^h\boldsymbol{\psi} - \boldsymbol{\psi})\cdot\boldsymbol{\nu}, 1\right\rangle_B = 0, \quad B = \Gamma_{jk} \text{ or } B = \Gamma_j.$$

The approximating properties of Π_{IJ}^h and Q^h are [14,20,22]

$$\|\boldsymbol{\varphi} - \Pi_{IJ}^h\boldsymbol{\varphi}\|_0 + h\|\boldsymbol{\varphi} - \Pi_{IJ}^h\varphi\|_1 \le Ch^{3/2}\|\boldsymbol{\varphi}\|_{3/2}, \tag{53}$$

$$\|\boldsymbol{\psi} - Q^h\boldsymbol{\psi}\|_0 \le Ch\|\boldsymbol{\psi}\|_1, \tag{54}$$

$$\|\nabla\cdot(\boldsymbol{\psi} - Q^h\boldsymbol{\psi})\|_0 \le Ch\left(\|\boldsymbol{\psi}\|_1 + \|\nabla\cdot\boldsymbol{\psi}\|_1\right). \tag{55}$$

The projection operators

$$\Pi_{66}^h : [H^{3/2}(\Omega_2)]^2 \to \mathcal{W}_{66}^h(\Omega_2), \qquad Q^h : H_0^1(\mathrm{div};\Omega_2) \to \mathcal{V}^h(\Omega_2)$$

are defined similarly and satisfy the approximating properties (53)–(55).

Now, we formulate the FE procedures to determine the stiffnesses p_{IJ}'s as follows:

- $p_{33}(\omega)$: find $\mathbf{u}^{(h,33)} \in \mathcal{Z}_{33}^h(\Omega)$ such that

$$\Lambda(\mathbf{u}^{(h,33)}, \mathbf{v}) = -\langle \Delta P, \mathbf{v}\cdot\boldsymbol{\nu}\rangle_{\Gamma^T}, \quad \forall \mathbf{v} \in \mathcal{Z}_{33}^h(\Omega). \tag{56}$$

- $p_{11}(\omega)$: find $\mathbf{u}^{(h,11)} \in \mathcal{Z}_{11}^h(\Omega)$ such that

$$\Lambda(\mathbf{u}^{(h,11)}, \mathbf{v}) = -\langle \Delta P, \mathbf{v}\cdot\boldsymbol{\nu}\rangle_{\Gamma^R}, \quad \forall \mathbf{v} \in \mathcal{Z}_{11}^h(\Omega). \tag{57}$$

- $p_{13}(\omega)$: find $\mathbf{u}^{(h,13)} \in \mathcal{Z}_{13}^h(\Omega)$ such that

$$\Lambda(\mathbf{u}^{(h,13)}, \mathbf{v}) = -\langle \Delta P, \mathbf{v}\cdot\boldsymbol{\nu}\rangle_{\Gamma^R\cup\Gamma^T}, \quad \forall \mathbf{v} \in \mathcal{Z}_{13}^h(\Omega). \tag{58}$$

- $p_{55}(\omega)$: find $\mathbf{u}^{(h,55)} \in \mathcal{Z}_{55}^h(\Omega)$ such that

$$\Lambda(\mathbf{u}^{(h,55)}, \mathbf{v}) = -\langle \mathbf{g}, \mathbf{v}_s\rangle_{\Gamma\setminus\Gamma^B}, \quad \forall \mathbf{v} \in \mathcal{Z}_{55}^h(\Omega). \tag{59}$$

- $p_{66}(\omega)$: find $\mathbf{u}^{(h,66)} \in \mathcal{Z}_{66}^h(\Omega_2)$ such that

$$\Lambda(\mathbf{u}^{(h,66)}, \mathbf{v}) = -\langle \mathbf{g}_2, \mathbf{v}_s\rangle_{\Gamma_2\setminus\Gamma_2^B}, \quad \forall \mathbf{v} \in \mathcal{Z}_{66}^h(\Omega_2). \tag{60}$$

Uniqueness for the FE procedures (56)–(60) can be shown with the same argument used for the continuous case. Existence follows from finite dimensionality.

6. *A priori* error estimates

In this section we derive the error estimates associated with the FE procedures (56)–(60).

Theorem 2. *Assume that* $\mathbf{u}_s^{(IJ)} \in [H^{3/2}(\Omega)]^2, \mathbf{u}_f^{(IJ)} \in H^1(\mathrm{div};\Omega)$ *for* $(I,J) = (1,1), (3,3), (1,3)$. *Also assume that the matrix* $\mathbf{E}$ *in* (36) *is positive definite. Then the following a priori error estimate holds:*

$$\begin{aligned}&\|\mathbf{u}_s^{(IJ)} - \mathbf{u}_s^{(h,IJ)}\|_1 + \|\mathbf{u}_f^{(IJ)} - \mathbf{u}_f^{(h,IJ)}\|_0 + \|\nabla\cdot(\mathbf{u}_f^{(IJ)} - \mathbf{u}_f^{(h,IJ)})\|_0\\ &\quad\le C(\omega)\left[h^{1/2}\|\mathbf{u}_s^{(IJ)}\|_{3/2} + h\left(\|\mathbf{u}_f^{(IJ)}\|_1 + \|\nabla\cdot\mathbf{u}_f^{(IJ)}\|_1\right)\right].\end{aligned} \tag{61}$$

Proof. First we analyze the error for the procedure (56) associated with determination of p_{33}.

Recall Korn's second inequality [21]:

$$\sum_{l,m=1,3} \|\epsilon_{lm}(\mathbf{v})\|^2 + \|\mathbf{v}\|_0^2 \geq C_1 \|\mathbf{v}\|_1^2, \quad \forall \mathbf{v} \in [H^1(\Omega)]^2. \tag{62}$$

Let L_* denote the minimum eigenvalue of the matrix $\mathbf{E}$. Then use (62) to see that the following Garding-type inequality holds:

$$\begin{aligned} \mathrm{Re}\,(\Lambda(\mathbf{v},\mathbf{v})) &= \mathrm{Re}\,((\mathbf{E}\,\widetilde{e}(\mathbf{v}),\widetilde{e}(\mathbf{v}))) \\ &\geq C_2\left(\|\mathbf{v}_s\|_1^2 + \|\nabla\cdot\mathbf{v}_f\|_0^2\right) - C_3\|\mathbf{v}_s\|_0^2, \end{aligned} \tag{63}$$

where

$$C_2 = \min\left(L_* C_1, 1\right), \quad C_3 = L_*.$$

Also, note that

$$\begin{aligned} &|\Lambda(\mathbf{u},\mathbf{v})| \leq C_4(\omega)(\|\mathbf{u}_s\|_1\|\mathbf{v}_s\|_1 + \|\nabla\cdot\mathbf{u}_f\|_0\|\mathbf{v}_s\|_1 + \|\mathbf{u}_s\|_1\|\nabla\cdot\mathbf{v}_f\|_0 \\ &\quad + \|\nabla\cdot\mathbf{u}_f\|_0\|\nabla\cdot\mathbf{v}_f\|_0 + \|\mathbf{u}_f\|_0\|\mathbf{v}_f\|_0) \\ &\quad \forall \mathbf{u} = (\mathbf{u}_s,\mathbf{u}_f) \in \mathcal{Z}_{33}^h, \mathbf{v} = (\mathbf{v}_s,\mathbf{v}_f) \in \mathcal{Z}_{33}^h. \end{aligned} \tag{64}$$

Set

$$\mathbf{e} = \mathbf{u}^{(33)} - \mathbf{u}^{(h,33)} \equiv (\mathbf{e}_s, \mathbf{e}_f). \tag{65}$$

Subtract (56) from (37) to obtain the error equation

$$\Lambda(\mathbf{e},\mathbf{v}) = 0, \quad \forall \mathbf{v} \in \mathcal{Z}_{33}^h. \tag{66}$$

Set

$$\boldsymbol{\Theta}^h(\mathbf{u}^{(33)}) = \left(\Pi_{33}^h \mathbf{u}_s^{(33)}, Q^h \mathbf{u}_f^{(33)}\right) \tag{67}$$

and take $\mathbf{v} = \mathbf{e} + \boldsymbol{\Theta}^h(\mathbf{u}^{(33)}) - \mathbf{u}^{(33)}$ in (66) to obtain the equation

$$\Lambda(\mathbf{e},\mathbf{e}) = \Lambda(\mathbf{e}, \mathbf{u}^{(33)} - \boldsymbol{\Theta}^h(\mathbf{u}^{(33)}). \tag{68}$$

Take imaginary part in (68) and use the approximating properties (53)–(55) to see that

$$\begin{aligned} \omega\left(\frac{\eta}{\kappa}\mathbf{e}_f, \mathbf{e}_f\right) &= \mathrm{Im}(\Lambda(\mathbf{e}, \mathbf{u}^{(33)} - \boldsymbol{\Theta}^h(\mathbf{u}^{(33)})) \\ &\leq |\Lambda(\mathbf{e}, \mathbf{u}^{(33)} - \boldsymbol{\Theta}^h(\mathbf{u}^{(33)})| \\ &\leq C_4(\omega)[\|\mathbf{e}_s\|_1\|\mathbf{u}_s^{(33)} - \Pi_{33}^h\mathbf{u}_s^{(33)}\|_1 + \|\nabla\cdot\mathbf{e}_f\|_0\|\mathbf{u}_s^{(33)} - \Pi_{33}^h\mathbf{u}_s\|_1 \\ &\quad + \|\mathbf{e}_s\|_1\|\nabla\cdot(\mathbf{u}_f^{(33)} - Q_h\mathbf{u}_f^{(33)}))\|_0 + \|\nabla\cdot\mathbf{e}_f\|_0\|\nabla\cdot(\mathbf{u}_f^{(33)} - Q_h\mathbf{u}_f^{(33)})\|_0 \\ &\quad + \|\mathbf{e}_f\|_0\|\mathbf{u}_f^{(33)} - Q_h\mathbf{u}_f^{(33)})\|_0] \\ &\leq C_5(\omega)[h^{1/2}\|\mathbf{u}_s^{(33)}\|_{3/2}(\|\mathbf{e}_s\|_1 + \|\nabla\cdot\mathbf{e}_f\|_0) \\ &\quad + h\|\nabla\cdot\mathbf{u}_f^{(33)}\|_1\left(\|\mathbf{e}_s\|_1 + \|\nabla\cdot\mathbf{e}_f\|_0\right) + h\|\mathbf{e}_f\|_0\|\mathbf{u}_f^{(33)}\|_1] \\ &\leq \delta_1(\|\mathbf{e}_s\|_1^2 + \|\nabla\cdot\mathbf{e}_f\|_0^2) + \delta_2\|\mathbf{e}_f\|_0^2 \\ &\quad + C_6(\omega)(h\|\mathbf{u}_s^{(33)}\|_{3/2}^2 + h^2(\|\mathbf{u}_f^{(33)}\|_1^2 + \|\nabla\cdot\mathbf{u}_f^{(33)}\|_1^2)). \end{aligned} \tag{69}$$

Then, choose δ_2 small enough in (69) to obtain the estimate

$$\|\mathbf{e}_f\|_0^2 \leq \delta_3\left(\|\mathbf{e}_s\|_1^2 + \|\nabla\cdot\mathbf{e}_f\|_0^2\right) + C_7(\omega)\left(h\|\mathbf{u}_s^{(33)}\|_{3/2}^2 + h^2\left(\|\mathbf{u}_f^{(33)}\|_1^2 + \|\nabla\cdot\mathbf{u}_f^{(33)}\|_1^2\right)\right). \tag{70}$$

Next, take real part in (68) and use (63) and the argument given above to derive the inequality (69) to obtain

$$\begin{aligned} C_2\left(\|\mathbf{e}_s\|_1+\|\nabla\cdot\mathbf{e}_f\|_0^2\right) &\leq \mathrm{Re}\left(\Lambda((\mathbf{e},\mathbf{u}-\boldsymbol{\Theta}^h)\right)+C_3\|\mathbf{e}_s\|_0^2\\ &\leq |\Lambda((\mathbf{e},\mathbf{u}-\boldsymbol{\Theta}^h)|+C_3\|\mathbf{e}_s\|_0^2\\ &\leq C_8(\omega)\Big[h^{1/2}\|\mathbf{u}_s^{(33)}\|_{3/2}\left(\|\mathbf{e}_s\|_1+\|\nabla\cdot\mathbf{e}_f\|_0\right)\\ &\quad+h\|\nabla\cdot\mathbf{u}_f^{(33)}\|_1\left(\|\mathbf{e}_s\|_1+\|\nabla\cdot\mathbf{e}_f\|_0\right)+h\|\mathbf{e}_f\|_0\|\mathbf{u}_f^{(33)}\|_1\Big]+C_3\|\mathbf{e}_s\|_0^2\\ &\leq \epsilon\left(\|\mathbf{e}_s\|_1^2+\|\nabla\cdot\mathbf{e}_f\|_0^2\right)+C_9(\epsilon,\omega)\left(h\|\mathbf{u}_s^{(33)}\|_{3/2}+h^2\left(\|\mathbf{u}_f^{(33)}\|_1^2+\|\nabla\cdot\mathbf{u}_f^{(33)}\|_1^2\right)\right)\\ &\quad+C_6(\epsilon,\omega)\left(\|\mathbf{e}_s\|_0^2+\|\mathbf{e}_f\|_0^2\right). \end{aligned} \tag{71}$$

Then, choose ϵ small enough in (71) to conclude that

$$\begin{aligned} \|\mathbf{e}_s\|_1^2+\|\nabla\cdot\mathbf{e}_f\|_0^2 &\leq C_{10}(\epsilon,\omega)\left(h\|\mathbf{u}_s^{(33)}\|_{3/2}+h^2\left(\|\mathbf{u}_f^{(33)}\|_1^2+\|\nabla\cdot\mathbf{u}_f^{(33)}\|_1^2\right)\right)\\ &\quad+C_{11}(\epsilon,\omega)\left(\|\mathbf{e}_s\|_0^2+\|\mathbf{e}_f\|_0^2\right). \end{aligned} \tag{72}$$

Next, we will employ a duality argument to estimate the $\|\mathbf{e}\|_0$-term in the right hand side of (72).

Let us solve the adjoint problem

$$\begin{aligned} &-i\omega\mathcal{B}\boldsymbol{\psi}-\mathcal{L}^*(\boldsymbol{\psi})=\mathbf{e},\\ &\boldsymbol{\sigma}(\boldsymbol{\psi})\boldsymbol{\nu}\cdot\boldsymbol{\nu}=0,\quad (x_1,x_3)\in\Gamma^T,\\ &\boldsymbol{\sigma}(\boldsymbol{\psi})\boldsymbol{\nu}\cdot\boldsymbol{\chi}=0,\quad (x_1,x_3)\in\Gamma,\\ &\mathbf{u}_s\cdot\boldsymbol{\psi}=0,\quad (x_1,x_3)\in\Gamma^L\cup\Gamma^R\cup\Gamma^B,\\ &\mathbf{u}_f\cdot\boldsymbol{\psi}=0,\quad (x_1,x_3)\in\Gamma. \end{aligned} \tag{73}$$

The following regularity will be assumed for the solution of (73) [19]:

$$\|\boldsymbol{\psi}_s\|_{3/2}+\|\boldsymbol{\psi}_f\|_1+\|\nabla\cdot\boldsymbol{\psi}\|_1\leq C(\omega)\|\mathbf{e}\|_0. \tag{74}$$

Thus, using integration by parts, for any $\mathbf{v}\in\mathcal{Z}_{33}^h$

$$\|\mathbf{e}\|_0^2=\left(\mathbf{e},-i\omega B\boldsymbol{\psi}-\mathcal{L}^*(\boldsymbol{\psi})\right)=\Lambda(\mathbf{e},\boldsymbol{\psi})=\Lambda(\mathbf{e},\boldsymbol{\psi}-\mathbf{v}). \tag{75}$$

Choose $\mathbf{v}=\left(\Pi_{33}^h\boldsymbol{\psi}_s,\,Q^h\boldsymbol{\psi}_f\right)$ in (75), use the approximating properties (53)–(55) and apply (74) to see that

$$\|\mathbf{e}\|_0^2\leq C_{12}(\omega)\Big[h^{1/2}\|\boldsymbol{\psi}_s\|_{3/2}\left(\|\mathbf{e}_s\|_1+\|\nabla\cdot\mathbf{e}_f\|_0\right)+h\|\nabla\cdot\boldsymbol{\psi}_f\|_1\left(\|\mathbf{e}_s\|_1+\|\nabla\cdot\mathbf{e}_f\|_0\right)+h\|\mathbf{e}_f\|_0\|\boldsymbol{\psi}_f\|_1\Big] \tag{76}$$

$$\leq C_{12}(\omega)\left(h^{1/2}\left(\|\mathbf{e}_s\|_1+\|\nabla\cdot\mathbf{e}_f\|_0\right)+h\|\mathbf{e}_f\|_0\|\mathbf{e}\|_0\right). \tag{77}$$

Hence,

$$\|\mathbf{e}\|_0\leq C_{12}(\omega)\left(h^{1/2}\left(\|\mathbf{e}_s\|_1+\|\nabla\cdot\mathbf{e}_f\|_0\right)+h\|\mathbf{e}_f\|_0\right). \tag{78}$$

Next, use (70) in (78) to obtain

$$\begin{aligned} \|\mathbf{e}\|_0^2 &\leq C_{13}(\omega)\left(h\left(\|\mathbf{e}_s\|_1^2+\|\nabla\cdot\mathbf{e}_f\|_0^2\right)+h^2\delta_3\left(\|\mathbf{e}_s\|_1^2+\|\nabla\cdot\mathbf{e}_f\|_0^2\right)\right)\\ &\quad+C_{14}(\epsilon,\omega)\left(h\|\mathbf{u}_s^{(33)}\|_{3/2}^2+h^2\left(\|\mathbf{u}_f^{(33)}\|_1^2+\|\nabla\cdot\mathbf{u}_f^{(33)}\|_1^2\right)\right). \end{aligned} \tag{79}$$

Employing the estimate (79) in (72) we conclude that

$$\begin{aligned} \|\mathbf{e}_s\|_1^2+\|\nabla\cdot\mathbf{e}_f\|_0^2 &\leq C_{15}(\omega)\left(h\|\mathbf{u}_s^{(33)}\|_{3/2}^2+h^2\left(\|\mathbf{u}_f^{(33)}\|_1^2+\|\nabla\cdot\mathbf{u}_f^{(33)}\|_1^2\right)\right)\\ &\quad+C_{11}(\omega)\left(h\left(\|\mathbf{e}_s\|_1^2+\|\nabla\cdot\mathbf{e}_f\|_0^2\right)+h^2\delta_3\left(\|\mathbf{e}_s\|_1^2+\|\nabla\cdot\mathbf{e}_f\|_0^2\right)\right). \end{aligned} \tag{80}$$

Then, choose δ_3 sufficiently small in (80) to get

$$\|\mathbf{e}_s\|_1^2 + \|\nabla\cdot\mathbf{e}_f\|_0^2 \leq C_{16}(\omega)\left(h\|\mathbf{u}_s^{(33)}\|_{3/2}^2 + h^2\left(\|\mathbf{u}_f^{(33)}\|_1^2 + \|\nabla\cdot\mathbf{u}_f^{(33)}\|_1^2\right)\right) + C_{11}(\omega)\left(h\left(\|\mathbf{e}_s\|_1^2 + \|\nabla\cdot\mathbf{e}_f\|_0^2\right)\right). \tag{81}$$

Thus, for h sufficiently small, from (81) we get the inequality

$$\|\mathbf{e}_s\|_1 + \|\nabla\cdot\mathbf{e}_f\|_0 \leq C_{17}(\omega)\left(h^{1/2}\|\mathbf{u}_s^{(33)}\|_{3/2} + h\left(\|\mathbf{u}_f^{(33)}\|_1 + \|\nabla\cdot\mathbf{u}_f^{(33)}\|_1\right)\right). \tag{82}$$

Finally, using (82) in (70) we conclude the validity of the error estimate (61) for the solution of (56). The error analysis for the solution of (57) and (58) follows with the same argument. This completes the proof.

The error analysis for the FE procedure (59) and (60) requires another argument because the solution vanishes on a set of positive measure of Γ. The following theorem states the estimates.

Theorem 3. *Assume that* $\mathbf{u}_s^{(55)} \in [H^{3/2}(\Omega)]^2, \mathbf{u}_f^{(55)} \in H^1(\text{div};\Omega)$ *and that* $\mathbf{u}_s^{(66)} \in [H^{3/2}(\Omega_2)]^2, \mathbf{u}_f^{(66)} \in H^1(\text{div};\Omega_2)$. *Also, assume that the matrix* $\mathbf{E}$ *in (36) is positive definite. Then for* $(I, J) = (5, 5), (6, 6)$ *the following a priori error estimate holds.*

$$\|u_s^{(IJ)} - u_s^{(h,IJ)}\|_1 + \|u_f^{(IJ)} - u_f^{(h,IJ)}\|_0 + \|\nabla\cdot(u_f^{(IJ)} - u_f^{(h,IJ)})\|_0 \leq C(\omega)\left[h^{1/2}\|u_s^{(IJ)}\|_{3/2} + h\left(\|u_f^{(IJ)}\|_1 + \|\nabla\cdot u_f^{(IJ)}\|_1\right)\right]. \tag{83}$$

Proof. Set

$$\mathbf{e} = \mathbf{u}^{(55)} - \mathbf{u}^{(h,55)} = (\mathbf{e}_s, \mathbf{e}_f). \tag{84}$$

Subtract (59) from (40) to obtain the error equation

$$\Lambda(\mathbf{e}, \mathbf{v}) = 0, \quad \forall \mathbf{v} \in \mathcal{Z}_{55}^h. \tag{85}$$

Set

$$\boldsymbol{\Theta}^h(\mathbf{u}^{(55)}) = \left(\Pi_{55}^h\mathbf{u}_s^{(55)}, Q^h\mathbf{u}_f^{(55)}\right) \tag{86}$$

and take $\mathbf{v} = \mathbf{e} + \boldsymbol{\Theta}^h(\mathbf{u}^{(55)}) - \mathbf{u}^{(55)}$ in (85) to obtain

$$\Lambda(\mathbf{e}, \mathbf{e}) = \Lambda(\mathbf{e}, \mathbf{u}^{(55)} - \boldsymbol{\Theta}^h(\mathbf{u}^{(55)}). \tag{87}$$

Next, recall that

$$\|\mathbf{v}\| = \left(\sum_{l,m=1,3}\|\epsilon_{lm}(\mathbf{v})\|^2\right)^{1/2} \tag{88}$$

defines a norm on $\{\mathcal{W}_{55}^h$ equivalent to the H^1-norm [20], i.e., there exist positive constants C_{11}, C_{12} such that

$$C_{18}\|\mathbf{v}\|_1 \leq \|\mathbf{v}\| \leq C_{19}\|\mathbf{v}\|_1, \quad \forall\ \mathbf{v} \in \mathcal{W}_{55}^h. \tag{89}$$

Hence,

$$\begin{aligned}\text{Re}\,(\Lambda(\mathbf{e}, \mathbf{e})) &= \text{Re}\,((\mathbf{E}\,\widetilde{e}(\mathbf{e}), \widetilde{e}(\mathbf{e})))\\ &\geq L_*\left(\|\mathbf{e}_s\|^2 + \|\nabla\cdot\mathbf{e}_f\|_0^2\right)\\ &\geq L_*\left(C_{18}\|\mathbf{e}_s\|_1^2 + \|\nabla\cdot\mathbf{e}_f\|_0^2\right).\end{aligned} \tag{90}$$

Then, take real part in (87) and use the approximating properties (53)–(55) to obtain

$$\begin{aligned} L_*\left(C_{18}\|\mathbf{e}_s\|_1^2+\|\nabla\cdot\mathbf{e}_f\|_0^2\right) &\le \mathrm{Re}\left(\Lambda(\mathbf{e},\mathbf{u}^{(55)}-\boldsymbol{\Theta}^h(\mathbf{u}^{(55)})\right)\le|\Lambda(\mathbf{e},\mathbf{u}^{(55)}-\boldsymbol{\Theta}^h(\mathbf{u}^{(55)})| \\ &\le C_{20}(\omega)\Big[h^{1/2}\|\mathbf{u}_s^{(55)}\|_{3/2}\left(\|\mathbf{e}_s\|_1+\|\nabla\cdot\mathbf{e}_f\|_0\right) \\ &\quad +h\|\nabla\cdot\mathbf{u}_f^{(55)}\|_1\left(\|\mathbf{e}_s\|_1+\|\nabla\cdot\mathbf{e}_f\|_0\right)+h\|\mathbf{e}_f\|_0\|\mathbf{u}_f^{(55)}\|_1\Big]. \\ &\le \epsilon\left(\|\mathbf{e}_s\|_1^2+\|\mathbf{e}_f\|_0^2+\|\nabla\cdot\mathbf{e}_f\|_0^2\right) \\ &\quad +C_{21}(\omega)\left(h\|\mathbf{u}_s^{(55)}\|_{3/2}^2+h^2\left(\|\mathbf{u}_f^{(55)}\|_1^2+\|\nabla\cdot\mathbf{u}_f^{(55)}\|_1^2\right)\right). \end{aligned} \tag{91}$$

Next, taking imaginary part in (87) and repeating the argument leading to (70) we see that the $\|\mathbf{e}_f\|_0$-term in the right-hand side of (91) satisfies the estimate

$$\|\mathbf{e}_f\|_0^2\le\delta_3\left(\|\mathbf{e}_s\|_1^2+\|\nabla\cdot\mathbf{e}_f\|_0^2\right)+C_7(\omega)\left(h\|\mathbf{u}_s^{(55)}\|_{3/2}^2+h^2\left(\|\mathbf{u}_f^{(55)}\|_1^2+\|\nabla\cdot\mathbf{u}_f^{(55)}\|_1^2\right)\right). \tag{92}$$

Next using (92) in (91), we obtain

$$\begin{aligned} L_*\left(C_{18}\|\mathbf{e}_s\|_1^2+\|\nabla\cdot\mathbf{e}_f\|_0^2\right) &\le \epsilon\left(\|\mathbf{e}_s\|_1^2+\|\nabla\cdot\mathbf{e}_f\|_0^2\right) \\ &\quad +C_{21}(\omega)\left(h\|\mathbf{u}_s^{(55)}\|_{3/2}^2+h^2\left(\|\mathbf{u}_f^{(55)}\|_1^2+\|\nabla\cdot\mathbf{u}_f^{(55)}\|_1^2\right)\right) \\ &\quad +\epsilon\left(\delta_3\left(\|\mathbf{e}_s\|_1^2+\|\nabla\cdot\mathbf{e}_f\|_0^2\right)\right. \\ &\quad \left.+C_7(\omega)\left(h\|\mathbf{u}_s^{(55)}\|_{3/2}^2+h^2\left(\|\mathbf{u}_f^{(55)}\|_1^2+\|\nabla\cdot\mathbf{u}_f^{(55)}\|_1^2\right)\right)\right). \end{aligned} \tag{93}$$

Thus, take ϵ and δ_3 small enough in (93) to derive the inequality

$$\|\mathbf{e}_s\|_1^2+\|\nabla\cdot\mathbf{e}_f\|_0^2\le C_{22}(\omega)\left[h\|\mathbf{u}_s^{(55)}\|_{3/2}^2+h^2\left(\|\mathbf{u}_f^{(55)}\|_1^2+\|\nabla\cdot\mathbf{u}_f^{(55)}\|_1^2\right)\right]. \tag{94}$$

Finally using (94) in (92) we conclude the validity of the error estimate (83) for $(I,J)=(5,5)$. The proof for $(I,J)=(6,6)$ is identical. This completes the proof.

7. Numerical experiments

The FE procedures described above are implemented to determine the five complex stiffnesses $p_{IJ}(\omega)$ as a function of frequency and the corresponding phase velocities and dissipation coefficients as indicated in Appendix B. In all the experiments the numerical samples were discretized using a 160×160 uniform mesh representing 10 periods of 15 cm background sandstone and 1 cm fracture thickness. Both background and fractures have grain density $\rho_s=2650$ kg/m^3, bulk modulus $K_s=37$ GPa and shear modulus $\mu_s=44$ GPa.

The dry bulk and shear moduli of the samples are determined by using the Krief model [23],

$$\frac{K_m}{K_s}=\frac{\mu}{\mu_s}=(1-\phi)^{3/(1-\phi)}. \tag{95}$$

Porosity is $\phi=0.25$ in the background and $\phi=0.5$ in the fractures. Using (95) we obtain $K_m=1.17$ GPa and $\mu=1.4$ GPa for the background and $K_m=0.58$ GPa and $\mu=0.68$ GPa for the fractures. Permeability is obtained as [24]

$$\kappa=\frac{r_g^2\,\phi^3}{45(1-\phi)^2} \tag{96}$$

where $r_g=20$ μm is the average radius of the grains, giving $\kappa=0.247$ D in the background and $\kappa=4.44$ D in the fractures.

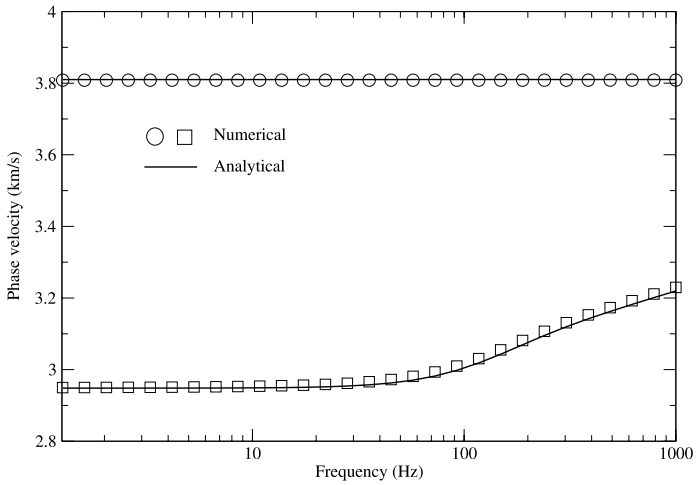

Fig. 2. P-wave velocity as a function of frequency in the direction parallel (squares and solid lines) and normal (circles and solid lines) to the fracture plane. The solid lines indicate the theoretical values.

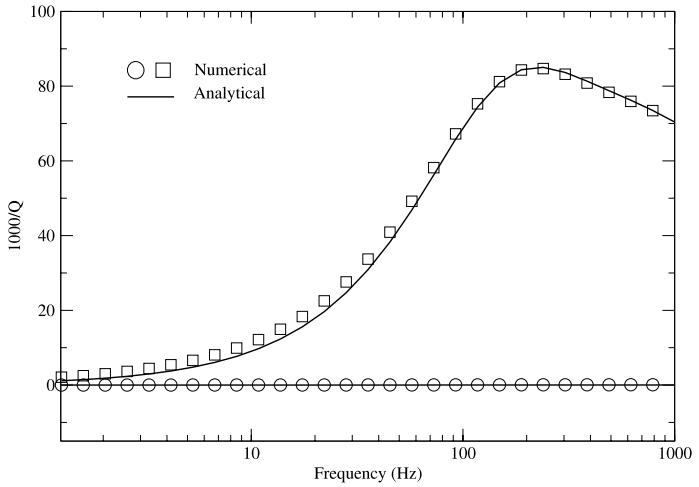

Fig. 3. P-wave dissipation factors as a function of frequency in the direction parallel (squares and solid lines) and normal (circles and solid lines) to the fracture plane. The solid lines indicate the theoretical values.

The first numerical experiments show the validation of the FE procedure by comparison with the analytical solution given in [7] which is included in Appendix A. In this example, we consider a brine saturated sample, with brine having a density of 1040 kg/m^3, a viscosity of 0.0018 Pa s and a bulk modulus of 2.25 GPa.

Figs. 2 and 3 show the compressional wave phase velocity and dissipation factor, respectively, as a function of frequency, in the direction parallel (squares and solid lines) and normal (circles and solid lines) to the fractures. The solid lines indicate the theoretical values, while symbols indicate the FE solution. It can be observed a perfect fit of the FE solution to the analytical values in the whole frequency range displayed.

The phase velocities of the qP, qSV and SH waves and dissipation factors of the qP and qSV waves as a function of the propagation angle are represented in Figs. 4 and 5, respectively, where the frequency is 300 Hz. Symbols and solid lines indicate the FE and theoretical values, respectively. Again an excellent match between the numerical and analytical curves is obtained for all angles. Here and in the following figures, the propagation angle is understood to be given with respect to the symmetry axis, so that 0° and 90° correspond to waves arriving normal and parallel to the fracture layering, respectively. Figs. 4 and 5 show that anisotropy induced by fractures is noticeable for the phase velocities of all waves. On the other hand, the qP curves show strong attenuation for waves arriving normal to the

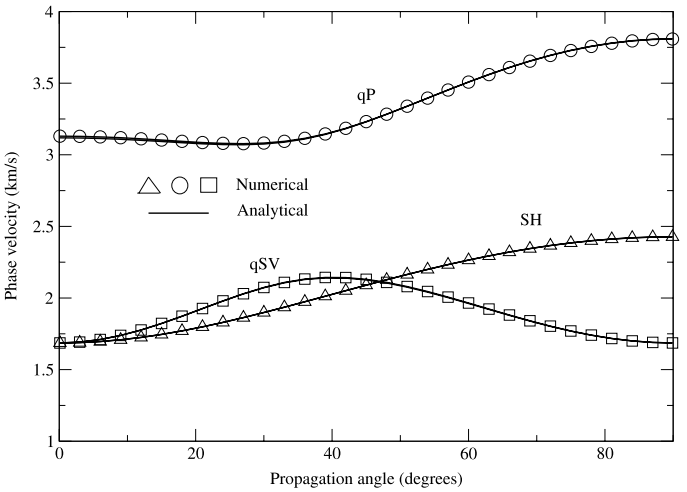

Fig. 4. Phase velocities for qP (circles), qSV (squares) and SH (triangles up) waves as function of the propagation angle. Frequency is 300 Hz. The solid lines indicate the theoretical values.

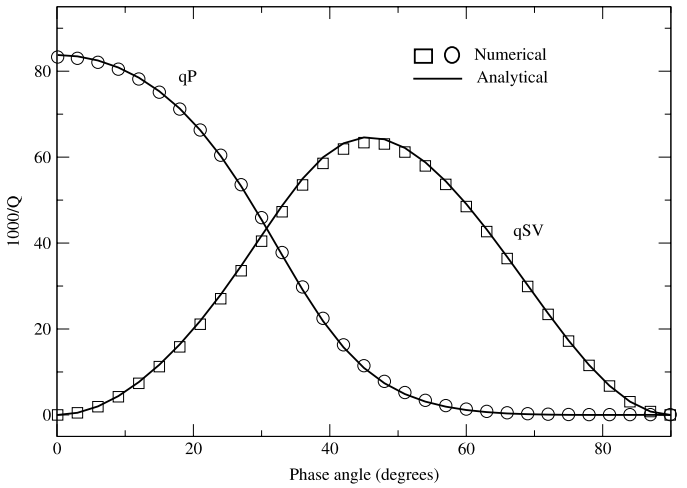

Fig. 5. Dissipation factors for qP (circles) and qSV (squares) waves as function of the propagation angle. Frequency is 300 Hz. The solid lines indicate the theoretical values.

fracture layering. The qSV wave has no loss along the directions parallel and perpendicular to the layering plane, showing maximum attenuation at about 45°.

Next, we present two experiments for which no analytical solutions are available. The first experiment considers the case of a patchy brine–CO_2 saturated fractured sample, with CO_2 having density 500 kg/m^3, viscosity $2 \cdot 10^{-5}$ Pa s and bulk modulus 22.5 MPa. To generate a patchy CO_2–brine saturation we use the von Karman self-similar correlation function for which the spectral density is given by [25]

$$S_d(r_x, r_z) = N_0(1 + R^2a^2)^{-(H+E/2)}. \tag{97}$$

Here, $R = \sqrt{r_x^2 + r_z^2}$ is the radial wavenumber, a the correlation length, H is a self-similarity coefficient ($0 < H < 1$), N_0 is a normalization constant and E is the euclidean dimension. The von Karman correlation (97) describes a self-affine, fractal processes of fractal dimension $D = E + 1 - H$ at a scale smaller than a. We choose $E = 2$, $D = 2.2$ and a to be 2.5% of the domain size. Once a continuous fractal distribution of brine is obtained over the 160×160 mesh, by properly chosen threshold values S_b^*, for each cell with brine saturation below and above S_b^* we assign to that cell either full CO_2 or full brine saturation, respectively. In this way we generated two different patchy

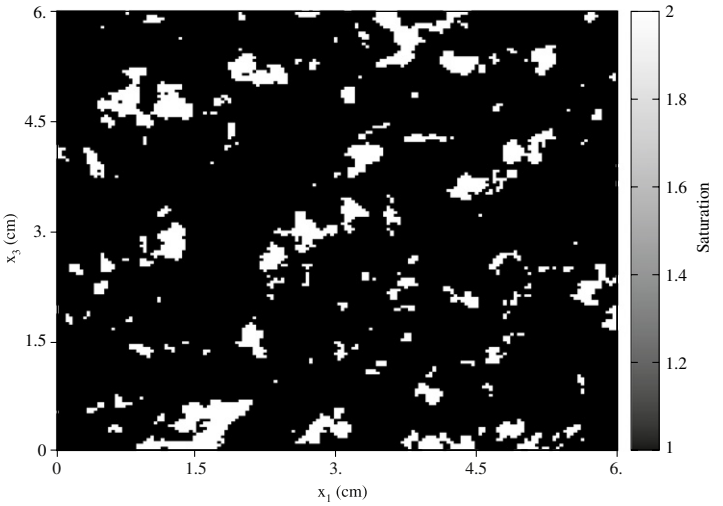

Fig. 6. Patchy CO_2–brine saturation. White zones correspond to full CO_2 saturation, and black ones to full brine saturation. The overall CO_2 saturation is 10%.

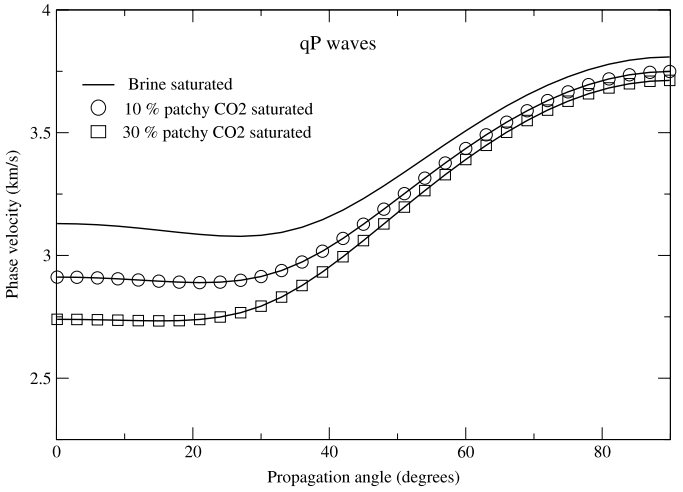

Fig. 7. qP phase velocities for brine, 10% and 30% patchy CO_2–brine saturation as function of the propagation angle. Frequency is 300 Hz.

CO_2-brine distributions of overall 10% and 30% CO_2 saturation. Fig. 6 displays the obtained patchy CO_2–brine saturation at 10% CO_2 saturation.

Figs. 7 and 8 show the phase velocities of the qP and qSV waves at 300 Hz for full brine saturation, 10% and 30% patchy CO_2-brine saturation as function of the propagation angle, while Figs. 9 and 10 show the corresponding dissipation factors.

It can be seen that for qP waves, patchy saturation enhances the strong velocity anisotropy caused by fractures observed in the brine saturated case, with values depending on the overall CO_2 saturation. Maximum differences with respect to the full brine saturation case are at 10% patchy saturation and angles normal to the fracture layering.

On the other hand, the qSV phase velocity anisotropy is less affected by patchy saturation. For both the qP and qSV waves we observe lower velocities when patches are present, with decreasing values for increasing CO_2 overall saturation. SH waves phase velocities are not affected by the presence of CO_2 patches, so the corresponding curve is identical to that for the full brine saturation in Fig. 4 and it is omitted.

Concerning the dissipation factors, the patchy saturation enhances attenuation anisotropy of the qP waves for all the angles and it is strong at 10% patchy saturation for waves arriving normal to the fracture layering plane and up to 30°. Above 60°, for the two cases of patchy saturation qP waves show an almost constant dissipation factor independently

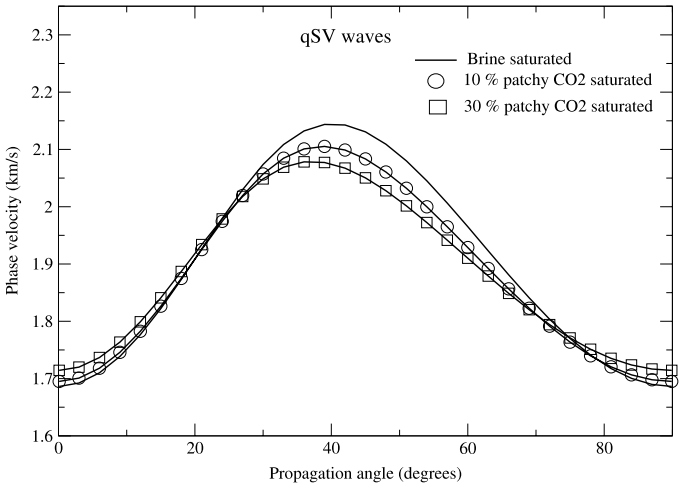

Fig. 8. qSV phase velocities for brine, 10% and 30% percent patchy CO_2-brine saturation as function of the propagation angle. Frequency is 300 Hz.

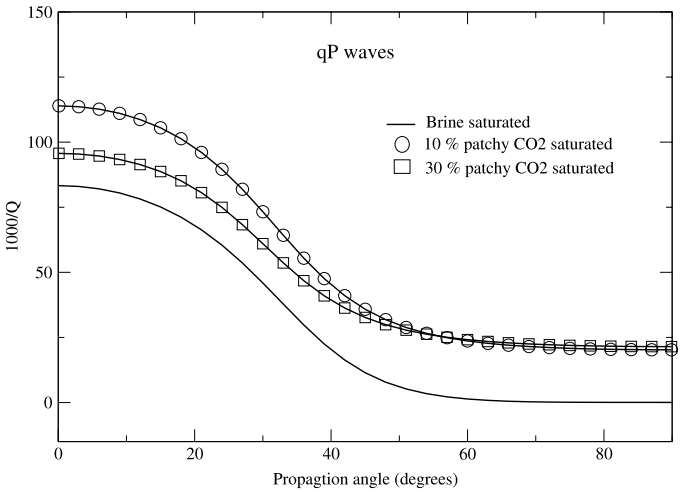

Fig. 9. Dissipation factors for brine, 10% and 30% patchy CO_2–brine saturation as function of the propagation angle. Frequency is 300 Hz.

of the value of CO_2 saturation. This is opposite to the case of full brine saturation, for which dissipation vanishes for angles above 60°.

For qSV waves, attenuation anisotropy is null for waves arriving normal or parallel to the fracture layering plane and strong for angles between 30 and 60°. Also, when compared with full brine saturation, dissipation factors are almost unaffected for 10% patchy saturation but noticeably reduced for the 30% CO_2 case.

Figs. 11 and 12 show the fluid pressure distribution for compressions normal to the fracture layering (p_{33} experiment) at frequency 300 Hz and for 10% and 30% patchy CO_2 saturation, respectively. The figure for 10% CO_2 saturation has larger regions of high pressure gradients than the 30% one, which explains the lower values of the dissipation factors for qP and qSV waves for 30% CO_2 saturation (squares) as compared with the corresponding curves for 10% CO_2 saturation (circles) in Figs. 9 and 10.

The second experiment considers the case of the brine saturated sample with uniform background as in the first set of experiments but with fractures having binary fractal variations in their petrophysical properties, which is another case not described by the theory in [7]. To generate such sample, first we generated a continuous fractal distribution of porosity over the mesh by using the spectral density in (97) with average $\overline{\phi}$ equal to 0.5, fractal dimension $D = 2.3$ and correlation length $a = 0.3$ in a scale of 10. In this way, we obtain minimum and maximum values of porosity of 0.32 and 0.646, respectively. Permeability is then computed using (96), giving values between 0.7 Darcy and 19

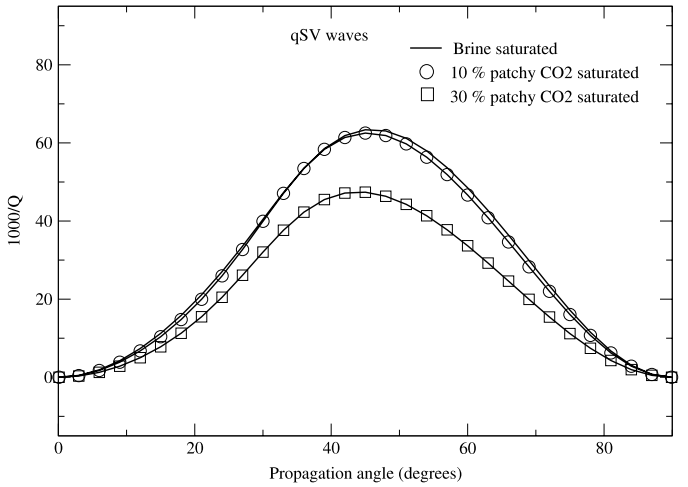

Fig. 10. Dissipation factors of qSV waves for brine, 10% and 30% patchy CO_2-brine saturation as function of the propagation angle. Frequency is 300 Hz.

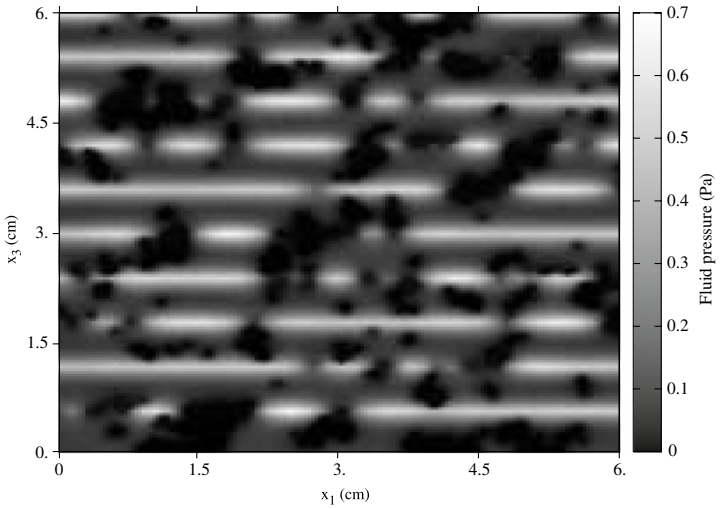

Fig. 11. Fluid pressure for normal compression to the fracture plane at 10% patchy CO_2–brine saturation. Frequency is 300 Hz.

Darcy, with an average of 4.9 Darcy. The binary fractals associated with porosity and permeability are then computed as follows. For each cell in the computational mesh, if the value of porosity is smaller (respectively, bigger) than the average $\overline{\phi}$, we assign to that cell the minimum (respectively, maximum) porosity value. The procedure is repeated to obtain a binary fractal permeability distribution. Binary fractal distributions of bulk modulus K_m and shear modulus μ are determined by using (95) and the computed binary fractal porosity field.

Taking 1D restrictions of these four binary fractal distributions for porosity ϕ, permeability κ, and bulk and shear moduli K_m and μ, we obtain the binary fractal petrophysical properties defining the brine saturated fractures.

Figs. 13–15 display the phase velocities of the qP, qSV and SH waves at 300 Hz as a function of the propagation angle for a brine saturated sample with uniform and binary fractal variations in the petrophysical properties of the fractures. Figs. 16–18 show the corresponding dissipation factors. It can be noticed a strong increase in velocity anisotropy for the three waves with respect to the case of uniform fractures. In particular, the qSV wave suffers a velocity reduction for almost all angles except near 40°and the phase velocity of the SH wave decreases by about 75%. Also, qP waves have a velocity increase for waves arriving at angles close to the normal to the fracture layering, and velocity decreases for all other angles. Regarding the dissipation factors, the qP waves show an increase in attenuation for angles up to 50°, while the qSV waves also show increasing attenuation for angles above 45°. The most significant

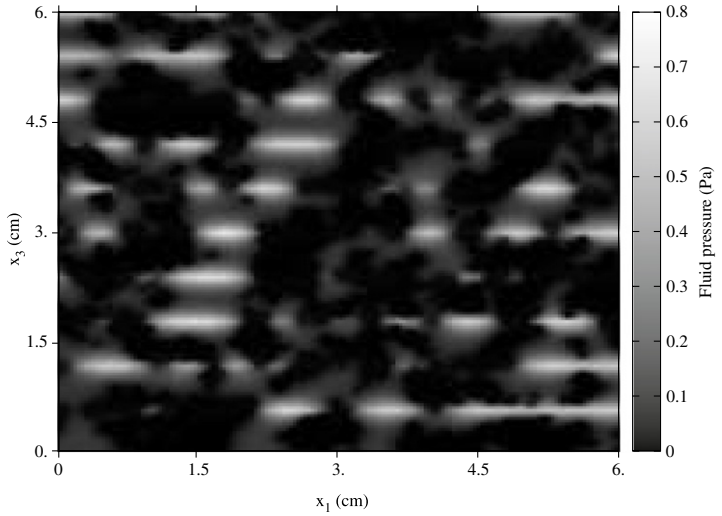

Fig. 12. Fluid pressure for normal compression to the fracture plane at 30% patchy CO_2–brine saturation. Frequency is 300 Hz.

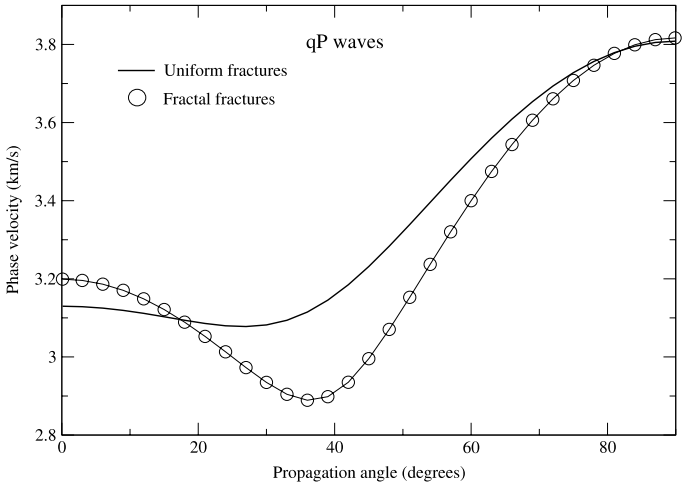

Fig. 13. Phase velocities of qP waves for a brine saturated sample with uniform and binary fractal fractures.

changes are observed in the SH dissipation factors, which change from vanishing dissipation to a continuous increase in dissipation for increasing angles.

8. Conclusions

We have presented a set of finite element harmonic experiments to determine the five complex and frequency-dependent stiffnesses of the TIV medium equivalent to a fractured fluid-saturated porous material, where the fractures are modeled as very thin, highly permeable and compliant porous layers. The procedure allows us to compute the wave velocities and quality factors at the macroscale as a function of frequency and propagation angle. The proposed methodology is based on the solution of the diffusive Biot equations in the space-frequency domain to simulate harmonic compressibility and shear tests. The methodology is validated against a theory valid at long wavelengths for homogeneous layers and fluid flow normal to the fracture layering.

Then, the experiments are applied for the cases of patchy brine–CO_2 saturation and a brine saturated sample of uniform background and fractures with fractal variations in their petrophysical properties. For the case of a patchy brine–CO_2 saturated sample, the experiments show that both for qP and qSV waves the presence of patches enhances the strong seismic velocity and attenuation anisotropy induced by the fractures. Also, SH waves show moderate

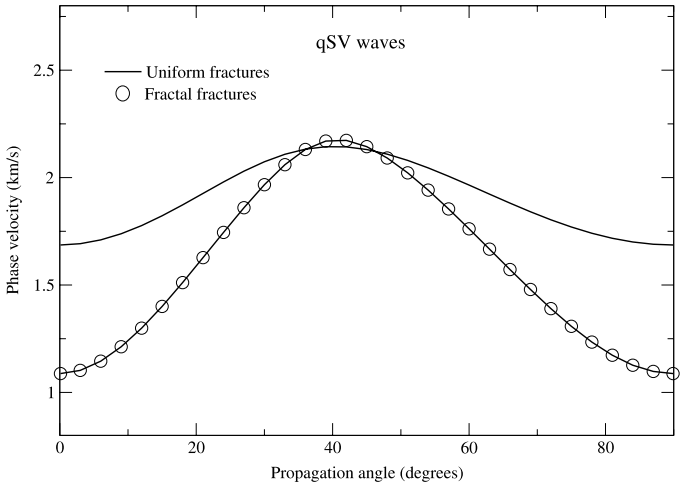

Fig. 14. Phase velocities of qSV waves for a brine saturated sample with uniform and binary fractal fractures.

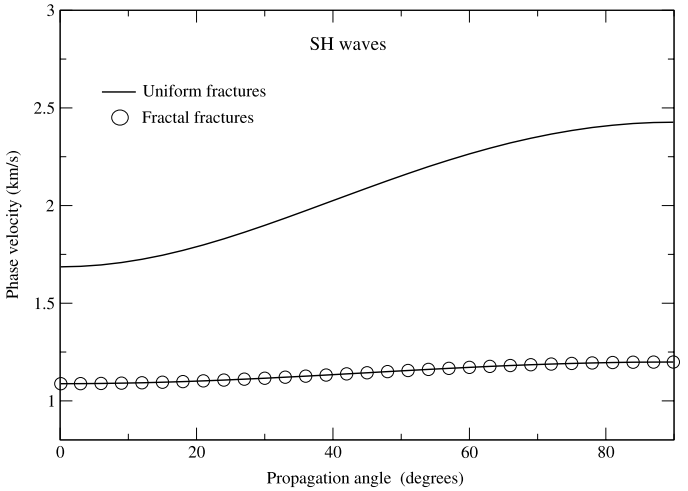

Fig. 15. Phase velocities of SH waves for a brine saturated sample with uniform and binary fractal fractures.

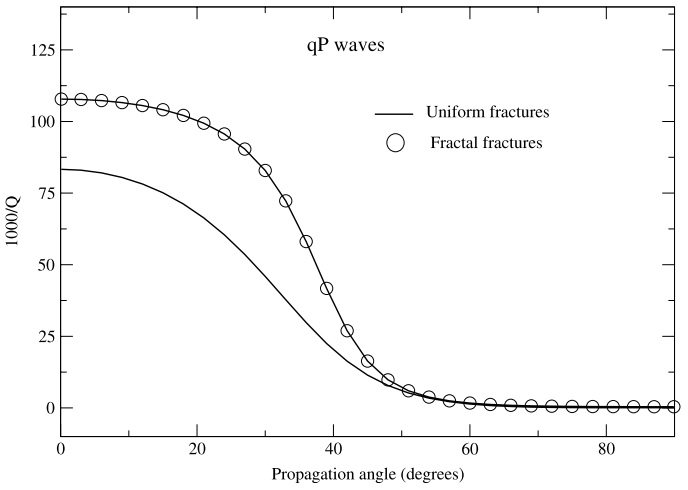

Fig. 16. Dissipation factors of qP waves for a brine saturated sample with uniform and binary fractal fractures.

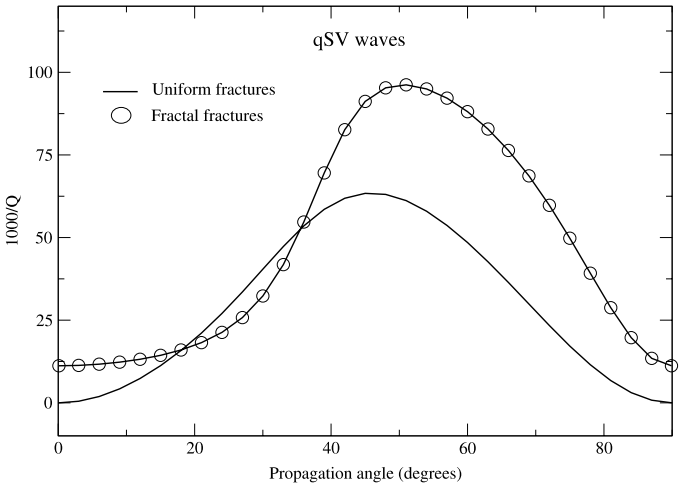

Fig. 17. Dissipation factors of qSV waves for a brine saturated sample with uniform and binary fractal fractures.

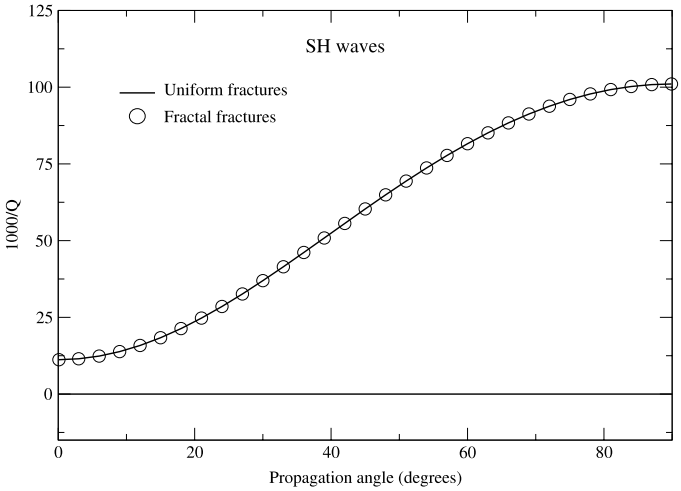

Fig. 18. Dissipation factors of SH waves for a brine saturated sample with uniform and binary fractal fractures.

velocity anisotropy, whose values are not affected by the presence of the patches of CO_2. In the last experiment, considering a brine saturated sample of uniform background and fractures of having fractal variations in petrophysical properties, it is observed a noticeable increase in velocity and Q anisotropy for all the waves, with higher dissipation factors as compared with the case of fractures of uniform properties. In particular, the SH dissipation factor shows positive and increasing values with increasing angles, as opposite to the uniform fractures case, which exhibits vanishing attenuation at all angles.

Acknowledgments

The work of J.E. Santos was partially funded by the GRANT PIP 112-20080100952 from CONICET, Argentina. J.M. Carcione has been partially funded by the CO2Monitor project.

Appendix A. Mesoscopic-flow attenuation theory for anisotropic poroelastic media

White's mesoscopic attenuation theory of interlayer flow [4,5] describes the equivalent viscoelastic medium of a stack of two thin alternating porous layers of thickness d_1 and d_2, such that the period of the stratification is $d = d_1 + d_2$. The theory gives the complex and frequency dependent stiffness p_{33}. White model has been generalized

in [7] by Krzikalla and Müller to anisotropic media, i.e., they have obtained the five stiffnesses of the equivalent transversely isotropic medium, denoted by p_{IJ}. The stress–strain relations is given by (6)–(11) and

$$p_{IJ}(\omega) = c_{IJ} + \left(\frac{c_{IJ} - c^r_{IJ}}{c_{33} - c^r_{33}}\right)[p_{33}(\omega) - c_{33}], \tag{A.1}$$

where c^r_{IJ} and c_{IJ} are the relaxed and unrelaxed stiffnesses.

According to Gelinsky and Shapiro [6] [their equation (14)], the quasistatic or relaxed effective constants of a stack of poroelastic layers are

$$\begin{aligned}
&c^r_{66} = B^*_1 = \langle \mu \rangle,\\
&c^r_{11} - 2c^r_{66} = c^r_{12} = B^*_2 = 2\left\langle \frac{\lambda_m \mu}{E_m}\right\rangle + \left\langle \frac{\lambda_m}{E_m}\right\rangle^2 \left\langle \frac{1}{E_m}\right\rangle^{-1} + \frac{B^{*2}_6}{B^*_8},\\
&c^r_{13} = B^*_3 = \left\langle \frac{\lambda_m}{E_m}\right\rangle \left\langle \frac{1}{E_m}\right\rangle^{-1} + \frac{B^*_6 B^*_7}{B^*_8},\\
&c^r_{33} = B^*_4 = \left\langle \frac{1}{E_m}\right\rangle^{-1} + \frac{B^{*2}_7}{B^*_8} = \left[\left\langle \frac{1}{E_m}\right\rangle - \left\langle \frac{\alpha}{E_m}\right\rangle^2 \left\langle \frac{E_G}{M E_m}\right\rangle^{-1}\right]^{-1},\\
&c^r_{55} = B^*_5 = \langle \mu^{-1} \rangle^{-1},\\
&B^*_6 = -B^*_8 \left(2\left\langle \frac{\alpha \mu}{E_m}\right\rangle + \left\langle \frac{\alpha}{E_m}\right\rangle \left\langle \frac{\lambda_m}{E_m}\right\rangle \left\langle \frac{1}{E_m}\right\rangle^{-1}\right),\\
&B^*_7 = -B^*_8 \left\langle \frac{\alpha}{E_m}\right\rangle \left\langle \frac{1}{E_m}\right\rangle^{-1},\\
&B^*_8 = \left[\left\langle \frac{1}{M}\right\rangle + \left\langle \frac{\alpha^2}{E_m}\right\rangle - \left\langle \frac{\alpha}{E_m}\right\rangle^2 \left\langle \frac{1}{E_m}\right\rangle^{-1}\right]^{-1},
\end{aligned} \tag{A.2}$$

where

$$\lambda_m = K_m - \frac{2}{3}\mu \quad \text{and} \quad E_m = K_m + \frac{4}{3}\mu \tag{A.3}$$

and we have also reported the notation of that paper for clarity. In the case of no interlayer flow, i.e., the unrelaxed regime, the stiffnesses are

$$\begin{aligned}
&c_{66} = c^r_{66},\\
&c_{11} - 2c_{66} = c_{12} = 2\left\langle \frac{(E_G - 2\mu)\mu}{E_G}\right\rangle + \left\langle \frac{E_G - 2\mu}{E_G}\right\rangle^2 \left\langle \frac{1}{E_G}\right\rangle^{-1},\\
&c_{13} = \left\langle \frac{E_G - 2\mu}{E_G}\right\rangle \left\langle \frac{1}{E_G}\right\rangle^{-1},\\
&c_{33} = \left\langle \frac{1}{E_G}\right\rangle^{-1},\\
&c_{55} = c^r_{55}
\end{aligned} \tag{A.4}$$

[Gelinsky and Shapiro [6], Eq. (15)], where

$$E_G = E_m + \alpha^2 M, \tag{A.5}$$

and M is given in (3).

Finally, the P-wave modulus p_{33} is [4], also see in [15]

$$p_{33} = \left[\frac{1}{c_{33}} + \frac{2(r_2 - r_1)^2}{\mathrm{i}\omega(d_1 + d_2)(I_1 + I_2)}\right]^{-1}, \tag{A.6}$$

where

$$r = \frac{\alpha M}{E_G} \tag{A.7}$$

and

$$I = \frac{\eta}{\kappa a}\coth\left(\frac{ad}{2}\right), \qquad a = \sqrt{\frac{\mathrm{i}\omega\eta E_G}{\kappa M E_m}}, \tag{A.8}$$

for each single layer.

The main assumption in [7] is that the fluid-flow direction is perpendicular to the fracture layering and that the relaxation behavior is described by a single relaxation function or stiffness, i.e., $p_{33}(\omega)$. Thus the theory is valid for plane layers and cannot be used when 2D or 3D heterogeneities are present.

Appendix B. Wave velocities and quality factors

We consider homogeneous viscoelastic waves [15]. The complex velocities are the key quantity to obtain the wave velocities and quality factor of the equivalent anisotropic medium. They are given by

$$\begin{aligned}
v_{\mathrm{qP}} &= (2\bar{\rho})^{-1/2}\sqrt{p_{11}l_1^2 + p_{33}l_3^2 + p_{55} + A},\\
v_{\mathrm{qSV}} &= (2\bar{\rho})^{-1/2}\sqrt{p_{11}l_1^2 + p_{33}l_3^2 + p_{55} - A},\\
v_{\mathrm{SH}} &= \bar{\rho}^{-1/2}\sqrt{p_{66}l_1^2 + p_{55}l_3^2},\\
A &= \sqrt{[(p_{11} - p_{55})l_1^2 + (p_{55} - p_{33})l_3^2]^2 + 4[(p_{13} + p_{55})l_1 l_3]^2},
\end{aligned} \tag{B.1}$$

where $\bar{\rho}$ is the average density, $l_1 = \sin\theta$ and $l_3 = \cos\theta$ are the directions cosines, θ is the propagation angle between the wavenumber vector and the symmetry axis, and the three velocities correspond to the qP, qS and SH waves, respectively. The phase velocity is given by

$$v_p = \left[\mathrm{Re}\left(\frac{1}{v}\right)\right]^{-1}, \tag{B.2}$$

while the quality factor is given by

$$Q = \frac{\mathrm{Re}(v^2)}{\mathrm{Im}(v^2)}, \tag{B.3}$$

where v represents either v_{qP}, v_{qSV} or v_{SH}.

References

[1] B. Gurevich, M. Brajanovski, R.J. Galvin, T.M. Müller, J. Toms-Stewart, P-wave dispersion and attenuation in fractured and porous reservoirs—poroelasticity approach, Geophys. Prospect. 57 (2009) 225–237.
[2] B. Gurevich, Elastic properties of saturated porous rocks with aligned fractures, J. Appl. Geophys. 54 (2003) 203–218.
[3] S. Picotti, J.M. Carcione, D. Gei, G. Rossi, J.E. Santos, Seismic modeling to monitoring CO_2 geological storage. The Atzbach–Schwanenstadt gas field, J. Geophys. Res. 117 (2012) B06103.
[4] J.E. White, N.G. Mikhaylova, F.M. Lyakhovitskiy, Low-frequency seismic waves in fluid saturated layered rocks, Phys. Solid Earth 11 (1975) 654–659.
[5] J.M. Carcione, S. Picotti, P-wave seismic attenuation by slow-wave diffusion, effects of inhomogeneous rock properties, Geophysics 71 (2006) O1–O8.

[6] S. Gelinsky, S.A. Shapiro, Poroelastic Backus-averaging for anisotropic, layered fluid and gas saturated sediments, Geophysics 62 (1997) 1867–1878.
[7] F. Krzikalla, T.M. Müller, Anisotropic P-SV-wave dispersion and attenuation due to interlayer flow in thinly layered porous rocks, Geophysics 76 (2011) W 135. http://dx.doi.org/10.1190/1.3555077.
[8] J.M. Carcione, B. Gurevich, J.E. Santos, S. Picotti, Angular and frequency dependent wave velocity and attenuation in fractured porous media, Pure Appl. Geophys. (2013) http://dx.doi.org/10.1007/s00024-012-0636-8.
[9] J.E. Santos, J.G. Rubino, C.L. Ravazzoli, A numerical upscaling procedure to estimate effective bulk and shear moduli in heterogeneous fluid-saturated porous media, Comput. Methods Appl. Mech. Engrg. 198 (2009) 2067–2077.
[10] S. Picotti, J.M. Carcione, J.E. Santos, D. Gei, Q-anisotropy in finely-layered media, Geophys. Res. Lett. 37 (2010) L06302.
[11] J.E. Santos, S. Picotti, J.M. Carcione, Evaluation of the stiffness tensor of a fractured medium with harmonic experiments, Comput. Methods Appl. Mech. Engrg. 247–248 (2012) 130–145.
[12] E.H. Saenger, R. Ciz, O.S. Krüger, S.M. Schmalholz, B. Gurevich, S.A. Shapiro, Finite-difference modeling of wave propagation on microscale: A snapshot of the work in progress, Geophysics 72 (2007) SM293–SM300.
[13] F. Wenzlau, J.B. Altmann, T.M. Müller, Anisotropic dispersion and attenuation due to wave-induced flow: quasi-static finite element modeling in poroelastic solids, J. Geophys. Res. 115 (2010) B07204. http://dx.doi.org/10.1029/2009JB006644.
[14] P.A. Raviart, J.M. Thomas, Mixed finite element method for 2nd order elliptic problems, in: Mathematical Aspects of the Finite Element Methods, in: Lecture Notes of Mathematics, vol. 606, Springer, 1975.
[15] J.M. Carcione, in: K. Helbig, S. Treitel (Eds.), Wave fields in real media: wave propagation in anisotropic, anelastic, porous and electromagnetic media, second ed., in: Handbook of Geophysical Exploration, vol. 38, Elsevier, Oxford, 2007, 515 pp.
[16] J.M. Carcione, Anisotropic Q and velocity dispersion of finely layered media, Geophys. Prospect 40 (1992) 761–783.
[17] H. Kolsky, Stress Waves in Solids, Dover publications, New York, 1963.
[18] R.A. Adams, Sobolev Spaces, Academic Press, 1975.
[19] B.E.J. Dahlberg, C.E. Kenig, G.C. Verchotta, Boundary value problems for the systems of elastostatics in Lipschitz domains, Duke Math. J. 57 (1988) 795–818.
[20] P.G. Ciarlet, The Finite Element Method for Elliptic Problems, Noth Holland, 1980.
[21] J.A. Nitsche, On Korn's second inequality, RAIRO 15 (1981) 237–249.
[22] J.C. Nedelec, Mixed finite elements in R^3, Numer. Math. 35 (1980) 315–341.
[23] M. Krief, J. Garat, J. Stellingwerff, J. Ventre, A petrophysical interpretation using the velocities of P and S waves (full waveform sonic), The Log Analyst 31 (1990) 355–369.
[24] J.M. Carcione, B. Gurevich, F. Cavallini, A generalized Biot–Gassmann model for the acoustic properties of shaley sandstones, Geophys. Prospect 48 (2000) 539–557.
[25] A. Frankel, R.W. Clayton, Finite difference simulation of seismic wave scattering: implications for the propagation of short period seismic waves in the crust and models of crustal heterogeneity, J. Geophys. Res. 91 (1986) 6465–6489.